# ABSTRACT

Title of dissertation: SUPPRESSION OF ELECTRON
THERMAL CONDUCTION IN
THE HIGH $\beta$ INTRACLUSTER
MEDIUM OF GALAXY CLUSTERS

Gareth Talbot Roberg-Clark
Doctor of Philosophy, 2019

Dissertation directed by: Professor James F. Drake
Department of Physics

Understanding the thermodynamic state of the hot intracluster medium (ICM) in a galaxy cluster requires a knowledge of the plasma transport processes, especially thermal conduction. The basic physics of thermal conduction in plasmas with ICM-like conditions has yet to be elucidated, however. We use particle-in-cell simulations and analytic models to explore the dynamics of an ICM-like plasma (with small gyroradius, large mean-free-path, and strongly sub-dominant magnetic pressure) induced by the diffusive heat flux associated with thermal conduction. Linear theory reveals that whistler waves are driven unstable by electron heat flux, even when the heat flux is weak. The resonant interaction of electrons with these waves then plays a critical role in scattering electrons and suppressing the heat flux. In a 1D model where only whistler modes that propagate parallel to the magnetic field are captured, the only resonant electrons are moving in the opposite direction to the heat flux and the electron heat flux suppression is small. In 2D or more, oblique whistler modes

also resonate with electrons moving in the direction of the heat flux. The overlap of resonances leads to effective symmetrization of the electron distribution function and a strong suppression of heat flux. The results suggest that thermal conduction in the ICM might be strongly suppressed.

In a numerical model with continually supplied heat flux in the system, two thermal reservoirs at different temperatures drive an electron heat flux that destabilizes off-angle whistler-type modes. The whistlers grow to large amplitude, $\delta B/B_0 \simeq 1$, and resonantly scatter the electrons. A surprise is that the resulting steady state heat flux is largely independent of the thermal gradient. The rate of thermal conduction is instead controlled by the finite propagation speed of the whistlers, which act as mobile scattering centers that convect the thermal energy of the hot reservoir. The results are relevant to thermal transport in high $\beta$ astrophysical plasmas such as hot accretion flows and the intracluster medium of galaxy clusters.

When the plasma $\beta$ is reduced in the numerical model, we find that a transition takes place between whistler-dominated (high-$\beta$) and double-layer-dominated (low-$\beta$) heat flux suppression. Whistlers saturate at small amplitude in the low $\beta$ limit and are unable to effectively suppress the heat flux. Electrostatic double layers suppress the heat flux to a mostly constant factor of the free streaming value once this transition happens. The double layer physics is an example of ion-electron coupling and occurs on a scale of roughly the electron Debye length. The scaling of ion heating associated with the various heat flux driven instabilities is explored over the full range of $\beta$ explored. The range of plasma-$\beta$s studied in this work makes it relevant to the dynamics of a large variety of astrophysical plasmas, including

not just the intracluster medium but hot accretion flows, stellar and accretion disk coronae, and the solar wind.

Suppression of electron thermal conduction in the high-$\beta$ intracluster
medium of galaxy clusters


by

Gareth Roberg-Clark


Dissertation submitted to the Faculty of the Graduate School of the
University of Maryland, College Park in partial fulfillment
of the requirements for the degree of
Doctor of Philosophy
2019


Advisory Committee:
Professor James Drake, Chair/Advisor
Professor Adil Hassam
Professor Thomas Antonsen, Jr.
Professor William Dorland
Professor M. Coleman Miller (Dean's Representative)

# Table of Contents

# List of Tables

# List of Figures

# List of Abbreviations

| | |
|---|---|
| AGN | Active Galactic Nucleus |
| DL | Double Layer |
| KAW | Kinetic Alfvén Wave |
| ICM | Intracluster Medium |
| MHD | Magnetohydrodynamics |
| PIC | Particle-In-Cell |

# Chapter 1:   Introduction

## 1.1   The Intracluster medium of galaxy clusters

### 1.1.1   Properties

A galaxy cluster is a collection of galaxies whose total mass is roughly $10^{14} -$ $10^{15}$ solar masses, with a spatial extent of $2-10~Mpc \sim 10^{23}~m$. Over 80% of the baryonic matter in a galaxy cluster resides in an atmosphere of hot plasma, the intracluster medium (ICM), which is in a state of approximate hydrostatic equilibrium within the gravitational potential of the cluster's dark matter halo. The ICM can be observed through x-rays produced via bremsstrahlung and sometimes houses bright radio sources known as AGN (Active Galactic Nuclei). Much of the plasma is in the form of hydrogen and helium [1]. The ICM plasma is rarefied ($n_e \sim 10^{-3} - 10^{-1}~\mathrm{cm}^{-3}$), very hot ($T \sim 10^7 - 10^8~\mathrm{K}$), and fully ionized.

### 1.1.2   ICM stability

Hydrodynamic stability in the ICM has been extensively studied. This is partly because many ICM cores (inner 100 kpc) have short cooling times ($t_{\mathrm{cool}} < 10^9~\mathrm{yr}$) and depressed temperatures [2]. If unchecked, the radiative losses in these cool-core

clusters would lead to significant accumulations of cold gas within the central galaxy, resulting in star formation rates of $100 - 1000\,\mathrm{M_\odot\,yr^{-1}}$, and central galaxies with stellar masses of $10^{13}\,\mathrm{M_\odot}$ or more [3]. Observed star formation rates and total stellar masses in these systems are an order of magnitude smaller, demonstrating that the radiative losses of the ICM must be largely offset. Early studies referred to this as the "cooling flow problem" since it was thought that large-scale inflows of thermal energy could maintain stability [2].

### 1.1.3   Roles of thermal conduction

Researchers in the 1970's speculated that thermal conduction from hot gas in the outer radii of clusters could provide the aforementioned offset, spurring them to add thermal fluxes to fluid models of the ICM. Some studies concluded, however, that thermal conduction would not strongly affect the equilibrium state of the cluster [4]. To this day it seems unclear whether thermal conduction significantly impacts hydrostatic equilibrium and it is unlikely that conduction will solve the problem by itself [5]. To match the observed profiles of clusters, fine-tuning of the relative strength of thermal conduction is required [6]. Given the high variability of the plasma conditions which set thermal conduction (both known and unknown), such fine-tuning seems unlikely to be at play in the ICM.

One proposed mechanism to combat radiative collapse of the ICM in cool-core clusters is AGN feedback, whereby a central galaxy/black hole system launches cool, accreted plasma back into the medium and then through some dissipative process

converts the kinetic energy of the outflow or jet into thermal energy [7]. Thermal conduction would be integral to many processes linked to AGN feedback. These processes are also of general importance to the dynamics of the plasma. Some examples include sound wave and shock dissipation [8, 9], the evaporation of cold clouds [10], and the behavior of fluid-like instabilities such as the heat flux driven buoyancy instability (HBI) [11] and magnetothermal instability (MTI) [12] which result in large-scale re-orientations of magnetic field in the presence of gravity and temperature gradients. Thermal conduction (or at least severe reduction of it) must also figure into the existence of so-called cold fronts (see a review by [13]) as well as optically radiating filaments in the outskirts of clusters [14]. As a result, thermal conduction should be well-understood in order to properly model galaxy clusters. Fortunately for us, this is not yet the case.

### 1.1.4   Transport in the magnetized ICM

The ICM is in an exotic regime of plasma physics. The first reason is that a relatively weak, tangled magnetic field pervades the ICM. The presence of the magnetic field is inferred through a variety of techniques such as Faraday rotation and synchrotron radiation measurements ( [15] and references therein). The magnetic field is weak in the sense that the ratio of the thermal pressure of the plasma to the magnetic field energy density is very large, $\beta \equiv 8\pi nT/B^2 \sim 100$. The second reason is that Coulomb collisions are infrequent. The electron mean free path is $\lambda \sim 0.1 - 1\,\mathrm{kpc}$ while the gyroradius, $\rho_e \sim 1\,\mathrm{npc}$, is many orders of magnitude

Table 1.1: Length scales in the ICM

| Length scale | Symbol | Size in meters |
|---|---|---|
| Cluster radius | $r_{cluster}$ | $10^{23}$ |
| Cool core radius | $r_{cc}$ | $10^{21}$ |
| Spatial res. of Perseus Cluster (0.4 arcsec) | $\delta x_{res}$ | $10^{19}$ |
| Mean free path (Coulomb) | $\lambda$ | $10^{16}$ |
| Electron gyroradius | $\rho_e$ | $10^7$ |
| Electron Debye length | $\lambda_{De}$ | $10^4$ |

smaller (see table 1.1). In this sense the ICM is strongly magnetized since individual particles can complete many gyrations about the magnetic field before they feel the effect of a collision on their orbit. As we shall see the "weak-strong" duality of the magnetic field has significant consequences for heat transport in the ICM.

When modeling thermal conduction in the ICM, most current treatments adopt a fluid description, taking the thermal conductivity to have the canonical Spitzer value [16] along the local magnetic field and complete suppression in the orthogonal direction. However, the Spitzer prescription assumes the plasma is strongly collisional on the spatial and time scales under consideration. This assumption can easily be violated in the ICM. Furthermore, the $\beta \gg 1$ ICM is likely susceptible to small-scale plasma instabilities driven by pressure anisotropies and heat fluxes which may impede thermal conduction [17]. In this thesis we explore an example

of such an instability and how it affects thermal conduction. Before describing the relevant physics we define what is meant by thermal conduction in a plasma and describe when the Spitzer assumptions break down.

## 1.2 Thermal conduction in plasmas

Thermal conduction refers to the transfer of heat energy resulting from the random (thermal) motions of constituent particles in a fluid or plasma. In this section we outline the basic assumptions used to model the process. We start with the Boltzmann equation and fluid closure of the moment equations (the historical treatment) and motivate study of the collisionless Boltzmann (Vlasov) equation. The goal is to discuss the heat flux vector $\mathbf{q}$ [see (1.9)], which is the primary component in thermal conduction.

### 1.2.1 Particle distribution functions

A plasma, consisting of many charged particles (electrons and ions) can be described by a phase-space distribution function $f(\mathbf{x}, \mathbf{v}, t)$ which takes the form of a probability distribution, where the spatial and velocity coordinates $(\mathbf{x}, \mathbf{v})$ are assumed to be independent of one another. When multiplied by the volume elements $d\mathbf{x}d\mathbf{v}$, the distribution function represents the probability that a particle can be found within $d\mathbf{x}d\mathbf{v}$.

### 1.2.2 The Boltzmann and Vlasov equations

The time evolution of the distribution function can be modeled by the Boltzmann equation,

$$\frac{\partial f}{\partial t} + \mathbf{v} \cdot \nabla_x f + \frac{\mathbf{F}}{m} \cdot \nabla_v f = \left(\frac{\partial f}{\partial t}\right)_{coll}, \tag{1.1}$$

where $\nabla_x = \partial/\partial\mathbf{x}$ and $\nabla_v = \partial/\partial\mathbf{v}$. $\mathbf{F}$ is the force that a particle of mass $m$ located at $(\mathbf{x}, \mathbf{v})$ would experience, ignoring small-scale fluctuating fields that might occur within a Debye sphere. We assume that $\mathbf{F}$ is the Lorentz force,

$$\mathbf{F} = e\left(\mathbf{E} + \frac{\mathbf{v}}{c} \times \mathbf{B}\right), \tag{1.2}$$

where $e$ is the particle charge, $\mathbf{E}$ is the electric field, and $\mathbf{B}$ is the magnetic field. The particle charge density and current density from $f$ feed into Maxwell's equations to evolve the fields.

The term on the right hand side of (1.1) represents the time evolution of the distribution function resulting from the small-scale fields ("collisions"). Note that a Boltzmann equation can be defined for each species in a plasma, including electrons and ions. The collision term is a summation over collisions between like and different species.

Taking the approximation that the system is completely free of collisions $[(\partial f/\partial t)_{coll} = 0]$, (1.1) yields the Vlasov equation,

$$\frac{\partial f}{\partial t} + \mathbf{v} \cdot \nabla_x f + \frac{\mathbf{F}}{m} \cdot \nabla_v f = 0, \tag{1.3}$$

which is the model that guides most of the work in this thesis. Assuming that the plasma is collisionless is to say that the collision frequency is much slower than any dynamical frequency of interest or that the collisional mean free path is much larger than the length scale of interest.

### 1.2.3 Moments of the Vlasov Equation: Heat Flux

It is often sensible to track the evolution of statistical quantities that vary in space by integrating out the velocity dependence of the distribution function. Multiplying (1.3) by various powers of $v$ and integrating over $d\mathbf{v}$ produces equations governing the time evolution of the so-called moments of the distribution function. Some important moments are the density

$$n = \int d\mathbf{v} f \tag{1.4}$$

and the mean flow

$$\mathbf{u} = \langle \mathbf{v} \rangle = \frac{1}{n} \int d\mathbf{v}\, \mathbf{v} f. \tag{1.5}$$

Three moment equations involving these quantities are

$$\frac{\partial n}{\partial t} + \nabla \cdot (n\mathbf{u}) = 0 \tag{1.6}$$

$$\frac{\partial}{\partial t}(mn\mathbf{u}) + m\nabla \cdot (n\mathbf{u}\mathbf{u}) + \nabla \cdot \mathbf{P} - en\left(\mathbf{E} + \frac{\mathbf{u}}{c} \times \mathbf{B}\right) = 0, \tag{1.7}$$

and

$$\frac{\partial}{\partial t}\left(\frac{1}{2}nm\mathbf{u}^2 + \frac{3}{2}p\right) + \nabla \cdot \left(\frac{1}{2}nm\mathbf{u}^2 + \frac{3}{2}p\right)\mathbf{u} + \nabla \cdot (\mathbf{P} \cdot \mathbf{u}) = -\nabla \cdot \mathbf{q} + ne\mathbf{E} \cdot \mathbf{u}. \tag{1.8}$$

Here we have defined the quantities

$$\text{p} = \left\langle \tfrac{1}{3}m(\mathbf{v} - \mathbf{u})^2 \right\rangle = nT \; (Scalar pressure)$$

$$\mathbf{P} = \langle m(\mathbf{v} - \mathbf{u})(\mathbf{v} - \mathbf{u}) \rangle \; (Pressure tensor) \text{ and the desired heat flux vector,}$$

$$\mathbf{q} = \left\langle \frac{1}{2}m(\mathbf{v} - \mathbf{u})(\mathbf{v} - \mathbf{u})^2 \right\rangle. \tag{1.9}$$

Reinserting (1.6) and (1.7), (1.8) becomes

$$\frac{\partial}{\partial t}\left(\frac{3}{2}p\right) + \nabla \cdot \left(\frac{3}{2}p\mathbf{u}\right) + \mathbf{P}{:}\nabla\mathbf{u} = -\nabla \cdot \mathbf{q}. \tag{1.10}$$

We see that the heat flux is an input to the energy equation (1.10). It is the flux of randomly directed kinetic energy, subtracting out any convection of this energy as a result of mean flows. Note that there is a time evolution equation for $\mathbf{q}$ that depends on the next moment of $f$. This dependence continues in an infinite hierarchy of moment equations. Rather than trying to tackle an infinite number of equations we can simply try to give $\mathbf{q}$ a specific form.

### 1.2.4 Thermal conduction from fluid closure

Here we briefly describe fluid models of thermal conduction for historical perspective and intuition. One can keep the collision term in (1.1) and make some headway in prescribing the heat flux and other moments.

### 1.2.4.1 Lowest order fluid closure

If the collisional mean free path is infinitely small compared to any relevant dynamical length scale (instead of infinitely large in the case of (1.3)), the distribution

becomes Maxwellian,

$$f = f_0 = \frac{n}{\pi^{3/2} v_T^3} \exp{-\frac{(\mathbf{v} - \mathbf{u})^2}{v_T^2}}, \tag{1.11}$$

where we have defined the thermal speed $v_T = (2T/m)^{1/2}$. Since only the first three moments of the distribution function, (1.6) - (1.8), are nonzero, this truncates the moment hierarchy by setting $\mathbf{q} = 0$.

### 1.2.4.2 Closure to first order

Alternatively, one can pin the collisionality at a finite level by taking the ratio

$$\epsilon = \frac{\lambda}{L} \ll 1 \tag{1.12}$$

where $\lambda$ is the collisional mean free path and $L$ is the dynamical length scale. Assuming (1.12) one can make an asymptotic closure of the moment equations. This is accomplished by writing

$$f = f_0 + \epsilon f_1, \tag{1.13}$$

the so-called Chapman-Enskog expansion [18]. The deviation $f_1$ is a response of the plasma to perturbations of the system, e.g. weak temperature gradients or electric fields. Integrating $f_1$ yields moments of the distribution function such as $\mathbf{q}$ (1.9).

### 1.2.4.3 Thermal conductivity coefficients

A consequence of (1.13) is that the heat flux is governed by a Fick's Law of diffusion,

$$\mathbf{q} = -\kappa \nabla T, \tag{1.14}$$

where $\kappa$ is the coefficient of thermal conductivity and depends on the properties of the plasma and interparticle collisions. The Spitzer coefficient of thermal conduction [16] scales like

$$\kappa_{sp} \sim \lambda^2 \nu_{ei} \sim \frac{T_e^{5/2}}{n_e} \tag{1.15}$$

where the electron-ion collision frequency is roughly

$$\nu_{ei} \sim \frac{Z^2 n_i \ln(\Lambda)}{m_e^{1/2} T_e^{3/2}} \tag{1.16}$$

and $\Lambda$ is the number of particles in a cube with Debye-length sides. $\ln(\Lambda)$ is known as the Coulomb logarithm and is $\sim 40$ for the ICM.

Hot plasma with Spitzer thermal conductivity conducts heat very well, while cool plasma does so poorly. 1.15 was derived assuming an unmagnetized plasma. In the context of a magnetized plasma such as the ICM, it turns out that thermal conduction in the direction of the local magnetic field is unchanged from 1.15 since $\mathbf{B}$ does not affect the parallel motion of particles. This allows one to use $\kappa_{sp}$ by projecting the temperature gradient in the $\hat{b} = \mathbf{B}/|\mathbf{B}|$ direction to obtain the parallel heat flux, $\mathbf{q}_\parallel = -\kappa_{sp}(\hat{b} \cdot \nabla T)\hat{b}$.

An expression for thermal conduction perpendicular to $\mathbf{B}$, $\kappa_\perp$, was provided by Braginskii [19]. Using the Chapman-Enskog scheme Braginskii found that

$$\kappa_\perp \sim \rho_e^2 \nu, \tag{1.17}$$

where $\rho_e = v_T/\Omega_e$ is the electron Larmor radius and $\nu$ is the collision frequency (to which both ion-electron and electron-electron collisions contribute). Since electron-ion and electron-electron collision times are comparable, the relative sizes of parallel

10

and perpendicular diffusion are $\kappa_\perp / \kappa_{sp} \sim \rho_e^2 / \lambda^2$. It is common in astrophysical contexts to assume that there is no diffusive heat flux perpendicular to $\mathbf{B}$ ($\kappa_\perp = 0$) because generally $\rho \ll \lambda \ll L$. Another prediction from Braginskii is that thermal fluxes tend to be dominated by the electron contribution, since it exceeds the ion heat flux by a factor of $(m_i / m_e)^{1/2}$. The combination of parallel thermal conduction using the Spitzer coefficient and negligible perpendicular diffusion is the standard approach for incorporating thermal fluxes into a fluid model. Our goal, however, is to treat the ICM plasma as collisionless and develop a new approach to solving the conduction problem.

### 1.2.5 Theories of collisionless thermal conduction

Previous work has recognized the possibility of collisionless effects playing an important role in thermal conduction in space and astrophysical plasmas. Examples include studies from the 1970s of collisionless plasma instabilities in the solar corona and solar wind (e.g. [20, 21]), in which it was recognized that skewed electron distribution functions carrying heat fluxes contained free energy for exciting collective motions (instabilities) of the plasma. In the nonlinear phase of their development, such instabilities could scatter particles in velocity space and constrain heat fluxes to marginally stable values as predicted by linear stability theory. Study of these instabilities was motivated by a growing number of in-situ space plasma measurements that did not match the predicted heat fluxes from the Spitzer prescription (e.g. [22]). This was an unsurprising trend since the collisional mean free path of

the solar wind is $\sim 1AU$, essentially the size of the entire earth-to-sun system.

In the context of clusters, Cowie & McKee added collisionless physics to their models in 1977 [10]. They imagined a half-Maxwellian plasma emitted from a hot boundary, which was in contact with a cold absorbing wall with no oppositely moving particles emitted or reflected from the boundary. Such a system requires a self-consistent electric field to be set up through Ampere's Law (note that $\nabla \times \mathbf{B} = 0$ in a 1D system). When this electric field is generated, it reflects some of the hot particles (to cancel the current) and reduces the overall heat flux. The result is assumed to be $q_{\parallel} \sim 0.4 v_T n T$. Cowie & Mckee called this the saturated heat flux. If the Spitzer prescription yields more heat flux than this (from a very strong temperature gradient), then something is wrong and $q$ must be capped to a fraction of the free-streaming value. A main result of this thesis is that the cap on heat flux is probably even more stringent in a high-$\beta$ plasma (Chapter 3). Other, more recent papers have considered the influence of relevant collisionless effects on thermal conduction in high-$\beta$ astrophysical plasmas such as the mirror and firehose instabilities [5,23,24], tangled magnetic field geometry [25], and magnetic field-line wandering [26]. Here we instead focus on how whistler waves can control thermal conduction.

## 1.2.6  Role of whistlers in limiting heat flux

Research in the 1990s began to suggest that the whistler wave (sec. 1.3) was a key player in astrophysical plasmas carrying thermal fluxes. For example, Levinson & Eichler [27] explored how the whistler instability can inhibit thermal

conduction along magnetic field lines and discussed their work within the context of the interstellar medium, although extensions to the ICM can be made. Pistinner & Eichler [28] also made some headway in the problem by discussing quasilinear effects and the necessity of including obliquely propagating whistlers to limit heat flux. Roughly simultaneous work by Gary et al. [29] suggested whistlers as a means of inhibiting thermal fluxes of electrons in the solar wind with extension to high-$\beta$ plasmas [30]. We also note here that recent shearing-box kinetic simulations imply that whistlers are commonplace in sheared accretion flows and can cause suppression of thermal conduction [31].

Levinson & Eichler's starting point was a form of the Chapman-Enskog scheme (1.13) previously employed by Ramani & Laval [32]. Ramani & Laval found that the resulting equilibrium (with a finite heat flux) from the Chapman-Enskog approach was in fact unstable and would produce fine-scale electromagnetic structures associated with the so-called Weibel instability [33, 34]. Levinson & Eichler arrived at a similar conclusion when they added a background magnetic field to the calculation, which did not change the equilibrium distribution function but did change the unstable modes generated by the heat flux to whistler waves. The works of Ramani & Laval and Levinson & Eichler showed what could happen if small-scale kinetic physics were introduced to fluid models of the system. These results set the stage for the approach taken in this thesis. In the next section we describe the basic physics of whistler waves.

## 1.3   Whistlers

### 1.3.1   Basic Description

Whistler waves were first observed as radio waves hitting antennae on earth. They are typically generated during lightning storms and can travel along the Earth's magnetic field, reaching the northern and southern poles. They are dispersive waves whose higher frequency constituents tend to travel faster. As a result, when converted to an audio signal they produce a descending-frequency sound that resembles a whistle. The basic whistler wave (a high-frequency extension of the fast mode from magnetohydrodynamics) propagates parallel to the local magnetic field $\mathbf{B}$ and is right-hand circularly polarized. The cold-plasma whistler dispersion relation for a parallel-propagating ($k_\parallel = k$) whistler, neglecting the displacement current in Maxwell's equations, reads

$$\omega(k) = \frac{k^2 d_e^2}{1 + k^2 d_e^2} \Omega_e, \tag{1.18}$$

where $d_e = c/\omega_{pe}$ is the electron skin depth, $\omega_{pe} = (4\pi n_0 e^2/m_e)^{\frac{1}{2}}$ is the plasma frequency and $\Omega_e = eB/(m_e c)$ is the electron cyclotron frequency. Here $n_0$ is the local electron density, $m_e$ is the electron mass, $c$ is the speed of light, and $e$ is the magnitude of the electron charge. The asymptotic value of the frequency (for $kd_e \to \infty$) is $\Omega_e$ so $\omega \Omega_e$. The whistler has a broad range of phase speeds but the characteristic speed assuming $kd_e \sim 1$ is $v_p = \omega(k)/k \sim d_e \Omega_e = V_{Ae}$, where $V_{Ae}$ is the electron Alfvén speed.

## 1.3.2 Resonance of electrons with whistler waves

Whistler dynamics are intimately connected to the behavior of electrons in magnetic fields. Since the parallel-propagating whistler is right-hand circularly polarized, the wave electric and magnetic fields rotate in the same sense as the lowest-order gyromotion of electrons around $\mathbf{B}$, allowing for resonant energy transfer between electrons and the wave. This resonant behavior drives linear wave growth and damping and underpins nonlinear phenomena such as trapping and scattering of electrons. In the 2D PIC simulations and theory presented in this thesis, it is the scattering by particles in resonance with whistlers which leads to suppression of heat flux in ICM-like plasmas.

### 1.3.2.1 Resonance condition for parallel-propagating whistlers

If a whistler propagates parallel to $\mathbf{B}$, the condition for an electron to be in cyclotron resonance with the wave is

$$\omega - kv_r - \Omega_e = 0, \tag{1.19}$$

where $v_r$ is the parallel resonant velocity. We show this by considering the equation of motion for an electron in the presence of a whistler. The total magnetic field in Cartesian coordinates is $\mathbf{B} = \mathbf{B_0} + \tilde{\mathbf{B}}$, where the background field is $\mathbf{B_0} = B_0 \hat{x}$ and $\tilde{\mathbf{B}} = \tilde{B} \left[ \cos(kx - \omega t)\hat{y} + \sin(kx - \omega t)\hat{z} \right]$ is the whistler magnetic field. The whistler has electric field components perpendicular to $B_0$ that are important but do not factor directly into this analysis. The equation of motion in the $x$ direction is

$$x = \frac{q}{mc} \left[ \mathbf{v}_\perp \times \mathbf{B} \right]_x \qquad (1.20)$$

We now assume that $\tilde{B} \ll B_0$ and insert the unperturbed orbit of an electron

rotating in the magnetic field $\mathbf{B_0}$, $\mathbf{v}_\perp = v_{\perp 0} \sin(\Omega_{e0}t)\hat{y} - v_{\perp 0} \cos(\Omega_{e0}t)\hat{z}$ and freely

streaming along the $x$ direction, $x = v_{x0}t$. Here $\Omega_{e0} = eB_0/(m_e c)$. (1.20) becomes

$$x = \Omega_{e0}\frac{\tilde{B}}{B_0}v_{\perp 0}\left[\sin(kv_{x0}t - \omega t)\sin(\Omega_{e0}t) + \cos(kv_{x0}t - \omega t)\cos(\Omega_{e0}t)\right]$$

$$= \Omega_{e0}\frac{\tilde{B}}{B_0}v_{\perp 0}\cos\left[(kv_{x0} - \omega + \Omega)t\right].$$

If one chooses $v_{x0} = v_r$ (equation 1.19) then the argument of the cosine in

(1.3.2.1) is zero and the acceleration that the particle feels is maximized and constant

in time. This is the resonance between the whistler and electron. The resonance

condition reveals the Doppler shift of the whistler rotation frequency by motion of

the electron along $\mathbf{B}$. Substituting (1.19) into (1.3.2.1) yields

$$v_r = -\frac{\Omega_e}{k(1 + k^2 d_e^2)} \qquad (1.21)$$

and so the electron must travel opposite the direction of wave propagation to be

resonant since the whistler frequency is less than the cyclotron frequency. Note that

a whistler traveling anti-parallel to $\mathbf{B}$ ($k < 0$) can be resonant with an electron with

positive parallel velocity.

## 1.3.2.2 Trajectories of resonant particles

An electron in resonance will oscillate within the wave fields of the whistler

and become trapped. A purely parallel-propagating whistler has no electric field

component parallel to **B** and its perpendicular electric field can be eliminated by transforming to a reference frame moving with the phase speed of the whistler along **B**. In this frame the remaining (magnetic) components of the whistler do no work on the electron and the electron kinetic energy is a conserved quantity. In the $v_{\parallel} - v_{\perp}$ phase space the electron orbit must therefore lie on a circle centered around $v_{\parallel} = v_p = \omega/k$. The electron executes trapped oscillations along this circle that are centered about the velocity $v_r$ [35]. The trapping process is described in detail in 2.4.

### 1.3.2.3 Energy transfer with a parallel whistler

While no energy transfer occurs in the whistler wave frame, some energy transfer will occur between the whistler and the electron in the laboratory frame since the two frames are shifted with respect to one another by $v_p$. In the limit of infinitesimally small wave amplitude, linear damping or growth of the wave occurs when the whistler interacts with a phase space distribution of electrons. The net contribution of energy to the wave (positive or negative) is found by integrating the distribution function over all resonant particles, taking into account the derivative of the distribution function along constant-energy contours [36, 37].

### 1.3.2.4 Obliquely propagating whistlers

Trapping of electrons can be greatly enhanced when whistlers propagate obliquely (at a finite angle) to the local magnetic field $\mathbf{B_0}$. In the oblique case, the whistler

becomes elliptically polarized. Since the wave phase that a particle sees now depends on the particle position perpendicular to $\mathbf{B_0}$, there are special cases in which the particle will see the whistler electric field rotating at integer multiples of its cyclotron motion about $B_0$. The resonance condition for an obliquely propagating whistler becomes

$$\omega - k_\parallel v_r - n\Omega_{e0} = 0, \tag{1.22}$$

where $n$ is the aforementioned integer multiple. Oblique propagation thus introduces resonances that can span a large region of phase space. The dynamics of the associated trapping motion around each resonance is mostly the same as in the parallel case. However, the crucial piece of physics introduced is that the regions of phase space associated with resonant trapped motion can overlap with one another given a sufficiently large wave amplitude [35, 38]. This is commonly referred to as resonance overlap or, in the language of nonlinear dynamics, the overlap of stochastic layers. As we shall see in the following chapters, resonance overlap is critical to the suppression of heat flux by whistlers.

## 1.4   Numerical method: Particle-In-Cell simulations

To probe the kinetic nonlinear physics of high-$\beta$ plasmas we model the constituent particles numerically. We carry out two-dimensional (2D) simulations using the particle-in-cell (PIC) code `p3d` [39] to model thermal conduction along an imposed temperature gradient in a magnetized, collisionless plasma. In `p3d` there are

macroparticles (each representing many actual particles) and electromagnetic fields $(\mathbf{E}, \mathbf{B})$. The macroparticles move through continuous space while the fields are evolved on a discrete grid. The macroparticles have their trajectories evolved using the relativistic Lorentz force equation

$$\frac{d(\gamma m \mathbf{v})}{dt} = q \left( \mathbf{E} + \frac{\mathbf{v}}{c} \times \mathbf{B} \right) \tag{1.23}$$

and the spatial step

$$\mathbf{v} = \frac{d\mathbf{x}}{dt}. \tag{1.24}$$

The fields are updated using the two Maxwell equations involving time derivatives (Faraday's Law and the Ampere-Maxwell Law), with the current density $\mathbf{J}$ calculated by interpolating particle velocities to the grid. The fields $(\mathbf{E}, \mathbf{B})$ are then interpolated back to the particle position to calculate the Lorentz force on the particle. This cycle then repeats.

## 1.5   Outline of Thesis

In Chap. 2, we study the stability of a plasma in which collisions and a large-scale temperature gradient have balanced each other out. We find that the system is whistler-unstable, consistent with earlier work [27, 28]. In 1D PIC simulations a modest suppression of heat flux occurs as the initial distribution function relaxes, while in 2D the suppression is markedly stronger. We link this behavior to cyclotron resonances occurring between electrons and whistlers. In a 1D system only a small region of phase space can interact with the parallel-propagating whistler. When

a large-amplitude oblique whistler develops in the 2D system, resonance overlap occurs and the entire phase space is subject to strong scattering, quenching heat flux. These simulations reveal the basic physics of heat flux suppression by whistlers.

In Chap. 3, we develop a new boundary condition to study a system with a continuous input of particles, driving a heat flux in a 2D system. In this case the same physics is at play as in Chap. 2, but the long-term evolution of the system comes to depend on the finite propagation speed of the whistlers. Electrons are also shown to diffuse in the presence of turbulent whistlers. Using analytic theory and looking at the spectrum of unstable waves we find a simple expression for the heat flux that suggests the maximum thermal conduction scales like $1/\beta$, the main result of the thesis.

In Chap. 4, we extend the theory to lower-$\beta$ systems to bring it into contact with observed plasmas in the solar wind. Through 2D PIC simulations with mobile ions we find that the dominant heat flux suppression at $\beta \sim 1$ is caused by electrostatic double layers. Since high-$\beta$ plasma is sometimes measured in the solar wind, the physics of whistler heat flux suppression could be important to the solar wind, which we continue to see in our simulations. We also find that a variety of mechanisms can lead to heating of ions in the full range of $\beta$ explored. These are examples of ion-electron coupling that are independent of Coulomb collisions.

In Chap. 5 we conclude the thesis.

Chapter 2:  Suppression of electron thermal conduction in the high-$\beta$

intracluster medium of galaxy clusters

In this chapter we explore the extension of fluid models of ICM-like plasma to the kinetic regime. In agreement with [27], we find that the fluid-type Chapman-Enskog equilibrium (derived from expression 1.13) breaks down and the system is unstable to whistler growth. We describe this process with linear analytic theory, finding that a low-frequency form of the whistler wave emerges in high $\beta$ systems. Most critical is the nonlinear physics of the interaction between the whistler and heat-carrying electrons, which leads to strong suppression of heat flux through overlap of resonances. We conclude that heat flux in the ICM may be significantly suppressed (1.15).

## 2.1  1D Instability Model

We solve the linearized Vlasov-Maxwell equations to obtain a dispersion relation for whistler-like modes propagating along the local magnetic field $\mathbf{B} = B_0 \hat{\mathbf{x}}$. The temperature $T$ is taken to be uniform but we include a heat flux as a source of free energy. We neglect ion terms, which scale like $\sqrt{m_e/m_i}$ and are small in simulations (not shown). Making the standard whistler assumptions, we obtain the

dispersion relation for the frequency $\omega$ of modes with wave vector $k$ along $\mathbf{B}$, [36]:

$$\frac{k^2 c^2}{\omega^2} - \frac{\omega_{pe}^2}{\omega n_0} \int d^3 \mathbf{v} \, \frac{v_\perp}{2} \frac{\left[ \left(1 - \frac{k v_x}{\omega}\right) \frac{\partial f_0}{\partial v_\perp} + \frac{k v_\perp}{\omega} \frac{\partial f_0}{\partial v_x} \right]}{\omega - k v_x - \Omega_e} = 0 \qquad (2.1)$$

where $\omega_{pe} = (4\pi n_0 e^2/m_e)^{1/2}$ is the plasma frequency, $\Omega_e = eB_0/m_e c$ is the cyclotron frequency, $f_0(\mathbf{v})$ is the initial electron phase space distribution, $v_{Te} = (2T_e/m_e)^{1/2}$ is the thermal speed, $\rho_e = v_{Te}/\Omega_e$ is the Larmor radius, $d_e = c/\omega_{pe}$ the skin depth and $\beta_e = 8\pi n_0 T_e/B^2$.

In the standard whistler ordering with $\omega \sim (k d_e)^2 \Omega_e \sim \Omega_e$ and $k d_e \sim 1$, waves in high beta plasmas resonate with bulk electrons, $v_x \sim \Omega_e/k \sim \Omega_e d_e \sim v_{Te}/\sqrt{\beta_e} \ll 1$, and are therefore heavily damped. Thus whistlers with conventional ordering do not exist in high beta plasmas. To obtain wave growth we consider longer wavelength modes with $\omega \sim (k d_e)^2 \Omega_e \ll \Omega_e$. Resonant particles have $v_x \sim \Omega_e/k \sim v_{Te}/(k\rho_e)$. Requiring $v_x v_{Te}$ yields $k\rho_e 1$ with $\omega \sim \Omega_e/\beta_e \ll \Omega_e$.

To model heat flux instability we use a distribution function from [27]

$$f_0(\mathbf{v}) = f_m \left[ 1 + \epsilon \left( \frac{v^2}{v_{Te}^2} - \frac{5}{2} \right) \frac{v_x}{v_{Te}} \right] \qquad (2.2)$$

where $f_m = n_{0e}/(\sqrt{\pi} v_{Te})^3 exp\left[-v^2/v_{Te}^2\right]$ and the term proportional to $\epsilon = v_{Te}/(\nu_{ei} L_T) \ll 1$ yields a heat flux (see also [32]). Equation 2.2 was obtained by balancing a large-scale temperature gradient (along $\mathbf{B_0}$) $\partial T/\partial x \equiv T/L_T$ with a Krook collision operator. $f_0$ has no net drift ($\langle \mathbf{v} \rangle = 0$) because a current-cancelling electric field was assumed to develop in steady state. The plasma pressure is also isotropic. The sole driver for instability is the heat flux, $q_{x0} = mn_0 \langle v_x v^2 \rangle/2 = (5/8)\epsilon mn_0 v_{Te}^3$. Using

22
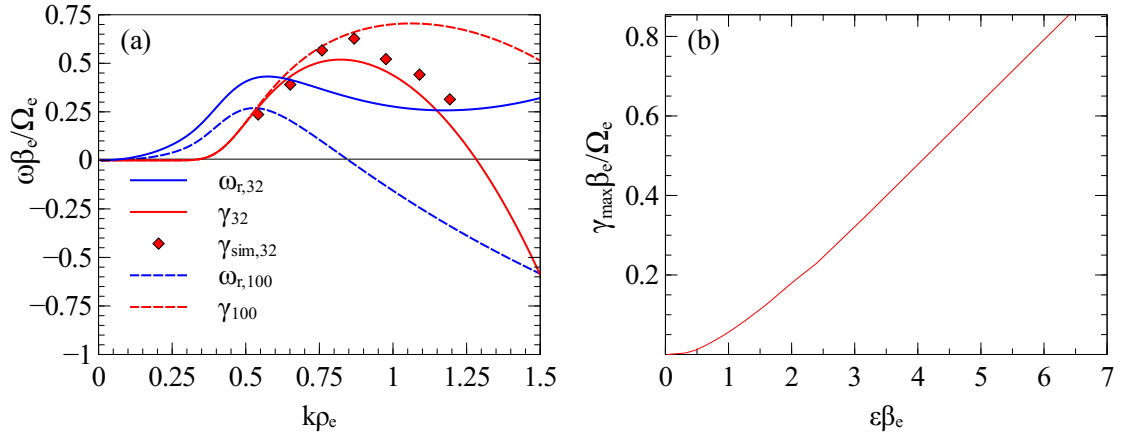
Figure 2.1: Analytic dispersion relation of the heat-flux-driven whistler-like wave in a plasma with $\beta_e = 32\,(solid), 100\,(dashed)$ and $\epsilon = 0.133$. (a) Real frequency (blue) and growth rate (red) of the instability calculated from Eq. (2.3). Red diamonds show growth rates at discrete values of $k$ taken from a 1D simulation with the same $\epsilon$ and $\beta = 32$. (b) Growth rate of the maximally growing mode for a range of $\epsilon\beta$.

this distribution function and taking $\omega \ll \Omega_e$ in Eq. 2.1 the frequency becomes

$$\omega = \frac{\Omega_e}{\beta_e} \left( k^2 \rho_e^2 + \epsilon \beta_e k \rho_e h_2 \right) \frac{1}{h_1}, \tag{2.3}$$

where

$$h_1(k\rho_e, \epsilon) = \frac{\Omega_e}{kn_0} \int d^3\mathbf{v} \frac{f_0}{v_x + \Omega_e/k} \tag{2.4}$$

and

$$h_2(k\rho_e) = \frac{1}{k\rho_e} \frac{1}{\epsilon} \int d^3\mathbf{v} \frac{v_x f_0 + (v_\perp^2/2)\partial f_0/\partial v_x}{v_x + \Omega_e/k}. \tag{2.5}$$

$h_2$ is only non-zero because of the heat flux and the integral over $v_x$ must go under the singularity at $v_x = -\Omega_e/k \equiv v_r$, the parallel resonant velocity. The real frequency $\omega_r$ and growth rate $\gamma$ versus $k$ for $\beta_e = 32, 100$ and $\epsilon = 0.133$ are presented in Fig. 2.1(a). The growth rate $\gamma$ is peaked around $k\rho_e \sim 1$ and goes to zero for small and large $k\rho_e$. The waves have whistler-like dispersion for small $k$ but the frequency rolls over at $k\rho_e \simeq 0.6$ and has a characteristic phase speed $v_{ph} = \omega/k \sim \rho_e \Omega_e/\beta_e = v_{Te}/\beta_e \ll v_{Te}$. The resonant interaction is with particles with $v_x \sim -v_r \sim -v_{te}$. In Fig. 2.1b the maximum growth rate (with respect to $k$) is plotted against $\beta\epsilon$. Instability exists for any non-zero value of $\epsilon$ so there is no threshold for the instability. This is highly relevant to the ICM, for which $\epsilon \ll 1$ [27]. We now present numerical simulations to verify (2.3) and to probe the impact on the heat flux.

## 2.2 PIC simulations

We simulate the instability using the particle-in-cell (PIC) code `p3d`. We present the results of quasi-1D, collisionless simulations (3600 particles per cell) with
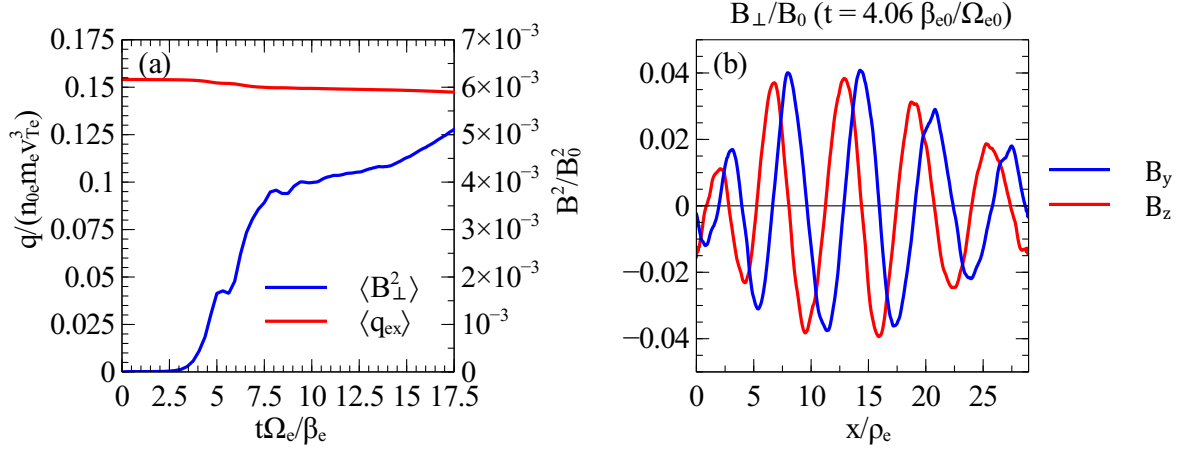
Figure 2.2: 1D PIC Simulation Results. (a) Average heat flux and mean squared value of the perturbed magnetic field. (b) Whistler-like phase relation between $B_y$ and $B_z$.

dimensions $L_x \times L_y = 28.96\rho_e \times 1.80\rho_e$ (a finite $L_y$ increases the number of particles and reduces particle noise) and a 2D simulation with $L_x \times L_y = 28.96\rho_e \times 28.96\rho_e$ (800 particles per cell). Periodic boundary conditions are used in both $x$ and $y$ with $\beta_{e0} = 32$. With these values of $L_x$ and $L_y$ many unstable modes of scale $\rho_e$ can fit in the box. Ions form a stationary, charge-neutralizing background.

There is no ambient temperature gradient but we initialize electrons with the distribution given in Eq. 2.2. Since $f_0$ is not strictly positive we adjust our initial distribution to ensure that $f_0 \geq 0$ and that it has no net drift or pressure anisotropy. Since $q_{x0}$ is also affected, we calculate an effective initial $\epsilon$ for comparison with the stability theory. Our 1D simulations are run to $t = 24.4 \; \beta_{e0}/\Omega_{e0}$ and a single 2D simulation is run to $t = 30.6 \; \beta_{e0}/\Omega_{e0}$.

## 2.3   1D Simulation Results

The 1D simulation, which has an effective $\epsilon = 0.246$, reveals that the heat flux drives waves unstable as predicted by Eq. 2.3. Magnetic fluctuations perpendicular to $\mathbf{B_0}$ grow in time (Fig. 2.2a) and saturate with $\tilde{B}_{sat} \simeq 0.1\, B_0$ . The waves are right-hand circularly polarized with $B_y$ and $B_z$ 90° out of phase (Fig. 2.2b). The linear growth rates from the simulation are in good agreement with those obtained from the linear theory (Fig. 2.1a).

The instability's nonlinear evolution coincides with a surprisingly weak reduction of the total heat flux (Fig. 2.2a). The reason for this behavior is linked to the mechanism by which whistlers gain energy from particles and are then scattered to reduce the heat flux. In the frame moving with the wave, particles move along concentric circles of constant energy (see Fig. 2.3d). Resonant electrons moving from high $v_\perp$ to low $v_\perp$ along the constant energy contour in the wave frame lose energy in the simulation frame. If more particles move in this direction than toward higher $v_\perp$, the waves grow. The portion of the distribution function proportional to $\epsilon$ in Eq. 2.2 and the associated heat flux are shown in Figs. 2.3a,b. Resonant particles that drive instability have $v_\perp > 1.5 v_{Te}$. This picture is confirmed in Fig. 2.3c, which shows the change in the electron distribution function as a result of the instability. Note the depletion of electrons with high $v_\perp$ and negative $v_x$. Saturation occurs when this relatively small region is depleted of excess particles. Figure 2.3b indicates that the bulk heat flux in phase space is carried by $v_x > 0$ particles with high energy, where the distribution function in Fig. 2.3c is essentially unchanged. Since positive
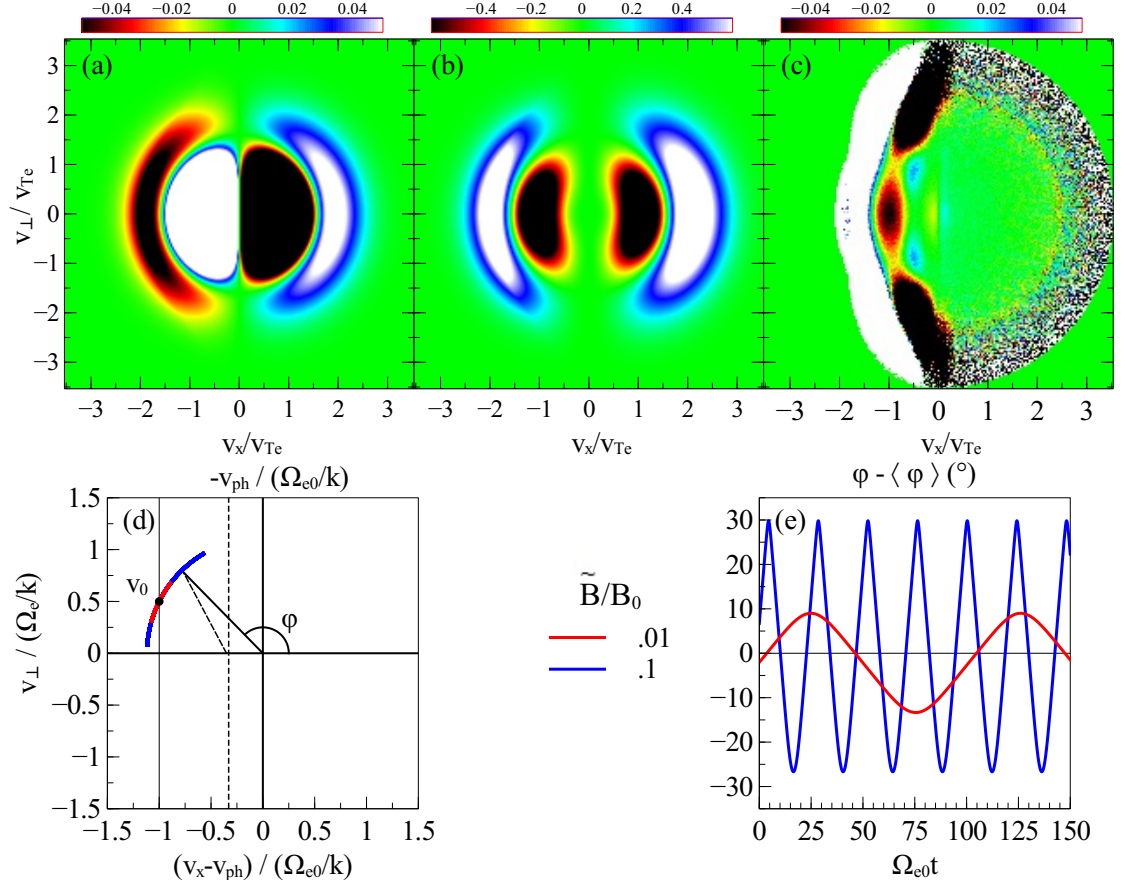
Figure 2.3: Phase space plots and particle trapping in 1D. (a) $(f_0 - f_M)/max(f_0 - f_M)$ from the PIC simulation. (b) The local heat flux, $(f_0 - f_M)v^2 v_x/max[(f_0 - f_M)v^2 v_x]$. (c) $\delta f/f_0 = (f - f_0)/f_0$ from the PIC simulation at late time, $t = 9.34\beta_{e0}/\Omega_{e0}$. (d) Trajectories of trapped test particles in the wave frame of the 1D whistler for small (red) and large (blue) $\tilde{B}$ (lab frame marked with dashed lines). The initial parallel velocity is the resonant velocity $-\Omega/k$. In (e) temporal evolution of the angle $\phi = \arctan(v_\perp/v_x)$ for the test particles in (d).

velocity electrons cannot resonate with the 1D whistler instability, significant heat flux suppression cannot occur.

## 2.4 1D Trapping Model

Modest heat flux reduction in 1D is linked to constraints on how electrons are scattered in a collisionless system. In 1D it is only electrons with velocity $v_x = -\Omega/k$ that resonantly drive the instability (Fig. 2.3c) and we will show that it is only particles close to this resonance that scatter. The substantial number of particles with $v_x > 0$, which carry the bulk of the heat flux (Fig. 2.3b,c), do not participate in heat flux suppression. The importance of resonant interactions and particle trapping in the scattering of particles by waves in magnetized plasma has been discussed by Karimabadi *et al*, 1992 based on a formal Hamiltonian theory [35].

We demonstrate this here by considering electrons in a whistler propagating in the positive $x$ direction, $\tilde{\mathbf{B}} = \tilde{B}(\hat{\mathbf{y}}\sin(kx - \omega t) + \hat{\mathbf{z}}\cos(kx - \omega t))$. In the frame moving with the whistler, the electric field is zero and the energy, $v_x^2 + v_y^2 + v_z^2 = v_0^2$, is conserved [35]. The equation of motion in the wave frame is

$$\frac{d\mathbf{v}}{dt} = -\Omega_e \mathbf{v} \times \hat{\mathbf{x}} - \Omega_e \frac{\mathbf{v} \times \tilde{\mathbf{B}}}{B_0}. \tag{2.6}$$

The fast time variation of the cyclotron motion can be eliminated by defining the new variables $v_\pm = (v_y \pm iv_z)e^{\mp i\Omega_e t}$,

$$\frac{dv_\pm}{dt} = v_x \tilde{\Omega}_e e^{\mp i(kx - \omega t)} \tag{2.7}$$

where $\tilde{\Omega}_e = e\tilde{B}/m_e c$. Shifting to a moving frame with velocity $-\Omega_e/k$, we define

$\bar{x} = x + \Omega_e t/k$ with $\bar{v}_x = v_x + \Omega_e/k$ so that Eq. 2.7 becomes

$$\frac{dv_\pm}{dt} = \left(\bar{v}_x - \frac{\Omega_e}{k}\right)\tilde{\Omega}_e e^{\mp ik\bar{x}} \tag{2.8}$$

with energy conservation now given by $v_+ v_- + (\bar{v}_x - \Omega_e/k)^2 = v_0^2$. The time variation of the particles in this frame is completely controlled by $\tilde{\Omega}_e$. The phase variation of the whistler, however, limits the excursion of $v_\pm$. As $v_\pm$ increases or decreases, $\bar{v}_x$ changes due to energy conservation and the wave phase $k\bar{x}$ changes even if $\bar{v}_x$ were initially zero. Consequently, the change in $v_\pm$ eventually reverses and the electrons are trapped (Fig. 2.3d). To show this, we take the time derivative of the energy relation and use Eq. 2.8 to obtain an equation for $\dot{\bar{v}}_x = \ddot{\bar{x}}$,

$$\ddot{\bar{x}} + \tilde{\Omega} v_\perp \cos(k\bar{x} + \phi) = 0, \tag{2.9}$$

where we have written $v_\pm = v_\perp e^{\pm i\phi}$. Because trapping limits the excursion of $v_\pm$ we can approximate $v_\perp$ and $\phi$ by their initial values $v_{\perp 0}$ and $\phi_0$. The equation for the phase angle $\theta = k\bar{x} + \phi_0 + \pi/2$ is

$$\ddot{\theta} + \omega_b^2 \sin\theta = 0, \tag{2.10}$$

where $\omega_b = \sqrt{k v_{\perp 0} \tilde{\Omega}_e}$ is the bounce frequency associated with deeply trapped particles. Integrating once yields

$$\frac{1}{2}\dot{\theta}^2 - \omega_b^2(1 - \cos\theta) = \frac{1}{2}\dot{\theta}_0^2 \tag{2.11}$$

where $\dot{\theta}_0$ is the value of $\dot{\theta}$ at $\theta = 0$. The maximum excursion of $\dot{\theta}$ corresponds to the separatrix in the phase space of $\theta - \dot{\theta}$ which is defined by $\dot{\theta}_0 = 0$. Thus, $\Delta\dot{\theta} = 2\omega_b$ is the trapping width. This corresponds to excursions

$$\frac{\Delta v_x}{v_r} = 2\sqrt{\frac{v_{\perp 0}}{v_r}\frac{\tilde{B}}{B_0}} \ll 1 \tag{2.12}$$

in $v_x$ and

$$\frac{\Delta v_\perp}{v_r} = 2\sqrt{\frac{v_r}{v_{\perp 0}}\frac{\tilde{B}}{B_0}} \ll 1 \tag{2.13}$$

in $v_\perp$, where $v_r = \Omega_e/k$. The same excursion was calculated for ions moving in circularly polarized Alfvén waves [40,41]. These bounds define the region in velocity space where electrons are scattered. Electrons outside of these ranges, which includes all of the positive velocity particles that carry the bulk of the heat flux, are not scattered [28].

To confirm the predictions of the trapping theory, we initialize a particle in the frame of a whistler-like wave in 1D with a resonant parallel velocity $v_x = -\Omega_e/k$. The particle trajectory in azimuthal angle $\phi = \arctan(v_\perp/v_x)$ in Fig. 2.3e reveals the trapped bounce motion. The corresponding excursion is shown in Fig. 2.3d. As predicted, both the frequency and amplitude of oscillations depend on $\tilde{B}/B_0$. Particles outside of resonance (not shown) exhibit only small amplitude oscillations.

## 2.5   2D Simulations and Analytic Theory

In contrast with the 1D simulations, the suppression of heat flux in 2D is substantial: for an initial $\epsilon = 0.246$ the heat flux decreases to $\approx 25\%$ of its starting value (Fig. 2.4a). Perturbations grow at a rate similar to those in the 1D case, have $k\rho_e \sim 1$, and propagate ($\omega/k \simeq v_{Te}/\beta_e$) along and perpendicular to the magnetic field (Fig. 2.4b) with a characteristic $k_\perp = k_y k_x$. The saturation time in 2D is only slightly longer than that in 1D. At $t\Omega_e/\beta_e \simeq 12.5$ the amplitude of magnetic perturbations reaches $0.4B_0$. A time sequence of $\delta f/f_0$ (Fig. 2.4d-g) shows the de-

velopment of resonances that were not present in the 1D system. Measured resonant velocities $v_{x,res}$ are a consequence of $k_\perp \neq 0$ (section 1.3.2.4) and are given by the condition $\omega - k_x v_x - n\Omega = 0$ where $n$ is any integer [35,36]. In particular, we observe that the $n = 1$ ($v_x < 0$), $n = 0$ ($v_x \simeq 0$) and $n = -1$ ($v_x > 0$) resonances all play crucial roles. At the point of saturation $f$ is significantly more isotropic in phase space than $f_0$ (not shown). Furthermore, the region of concentrated heat flux in Figure 2.4b ($v_x v_{Te}$) has been drained of excess particles. Whereas in 1D the trapping mechanism was unable to significantly reduce the heat flux, in 2D the availability of the $n = 0$ and $n = -1$ resonances and resonant overlap allow trapping to drive strong pitch-angle scattering over a broad range of velocities [28]. This scattering isotropizes the distribution function by connecting the $v_x < 0$ and $v_x > 0$ regions of phase space.

Trapping equations in the 2D case were derived in [42] and the results are similar in form to (2.10) and (2.11). The results for the $n = 0$ (Landau) and $n = \pm 1$ (Cyclotron) resonances are nearly identical to the 1D case and have the form of Equation 2.10, where $\omega_b \simeq \sqrt{k v_{\perp 0} \tilde{\Omega}_e}$. To demonstrate the importance of these resonances, we evaluate test particle orbits in the reference frame of a 2D off-angle whistler wave. In this frame the wave takes the form

$$\mathbf{B} = B_0 \hat{\mathbf{x}} + \tilde{B} \left[ \left( -\frac{k_y}{k_x} \hat{\mathbf{x}} + \hat{\mathbf{y}} \right) \sin(k_x x + k_y y) + \frac{k}{k_x} \hat{\mathbf{z}} \cos(k_x x + k_y y) \right] \tag{2.14}$$

where $\tilde{B}_x \neq 0$ and the wave is elliptically, rather than circularly, polarized. In evaluating the particle orbits we take $k_y = k_x$ and consider two different values for $\tilde{B}/B_0$: 0.05 and 0.4. Particles are initialized with parallel velocities at the $n = 0, \pm 1$
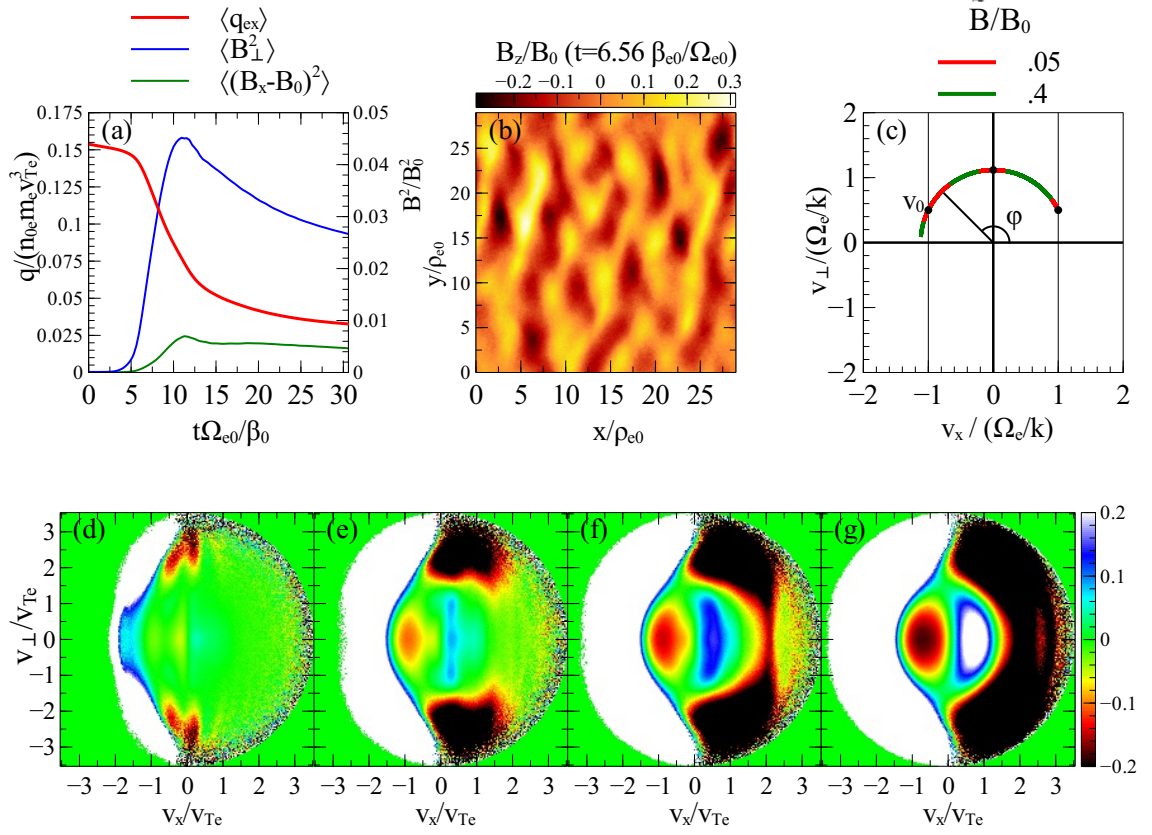
Figure 2.4: 2D simulation results and trapping theory. (a) Averages of the heat flux and mean-squared values of the perturbed perpendicular and parallel magnetic fields versus time. (b) The 2-dimensional structure of the magnetic field $B_z$. (c) In the wave frame of a 2D whistler, the orbits of trapped test particles for two values of $\tilde{B}$. The $v_x - v_\perp$ phase space of $\delta f/f_0 = (f - f_0)/f_0$ at $t\Omega_{e0}/\beta_{e0} = 5.31$ (d), 8.12 (e), 10.94 (f), and 30.6 (g).

resonances. In the case of $\tilde{B}/B_0 = 0.05$ we find that trapping widths are small, as predicted by the nonlinear theory (Figure 2.4c). However, when $\tilde{B}/B_0 = 0.4$, a particle starting at $v_x = \Omega_e/k$ experiences strong trapping and is scattered into the domains of the other two resonances, reversing its original parallel velocity. This is consistent with the results of [35], in which it was found that resonant overlap occurs when $\delta B/B_0 \simeq 0.3$. It is not a coincidence that saturation takes place once perturbed amplitudes of this size are reached, for it is by this mechanism, in which particles are "handed off" between different resonances, that the particles driving instability are scattered in phase space and wave growth ceases.

## 2.6  Conclusions

We have shown using both PIC simulations and linear theory that low-frequency $(\omega \sim \Omega_e/\beta_e)$ whistler-like modes in a high-$\beta$ collisionless plasma are driven unstable by thermal heat flux, even when the pressure is isotropic. The non-linear suppression of the heat flux is negligible in 1D, but becomes substantial in 2D owing to overlapping Landau and cyclotron resonances that lead to effective scattering of electrons. This strong suppression of thermal heat fluxes may be important for understanding the thermodynamics of the ICM in galaxy clusters.

In order to quantify the astrophysical importance of these effects, we attempt to calculate an effective thermal conductivity for the ICM. The electron distribution function was earlier calculated by balancing the background temperature gradient with a Krook collision operator, producing the distribution function given in

Eq. (2.2), where the term proportional to $\epsilon = v_{Te}/\nu_{ei}L_T$ describes the heat flux [27]. Although we have not carried out a scaling study of the rate of wave-driven electron scattering $\nu_w$ with parameters, a reasonable hypothesis is that $\nu_w$ is given by the peak linear growth rate $\nu_w = \gamma = \epsilon\Omega_e$. Repeating the heat flux calculation by replacing $\nu_{ei}$ with $\nu_w$ yields $\epsilon = \sqrt{\rho_e/L_T}$ and a heat flux $q_\parallel$ given by

$$q_\parallel \propto v_{te}nT_e\sqrt{\frac{\rho_e}{L_T}}. \tag{2.15}$$

This is reduced from the collisionless, free-streaming value by the factor $\sqrt{\rho_e/L_T}$, which can be as small as $10^{-6}$ for the ICM. However, we caution that (2.15) has been supplanted by expression (3.3) which we find in the next chapter and which makes a qualitatively different prediction about thermal conduction.

A caveat is that our numerical models are run with large heat fluxes ($\epsilon \approx 0.25$) whereas typical heat fluxes in the ICM can be much smaller. While linear theory shows that the whistler instability exists for any non-zero heat flux, it is possible that there exists a threshold heat flux below which whistler-mediated scattering of electrons is ineffective. On the other hand, our present simulations are initial value problems that relax to an equilibrium system in a periodic box, while a more realistic configuration would continually drive a heat flux down a temperature gradient, explicitly linking heat flux and temperature gradient. The unlimited supply of free energy into the system would likely drive the large-amplitude perturbations that satisfy the resonance overlap condition, $\delta B/B_0 0.3$, regardless of how small the driving heat flux is. This will likely lead to a saturated state in which injection and disruption of heat flux balance and so differ significantly from that of the initial

value problem in which heat flux relaxes to a low level. In the next chapter we explore such a model.

# Chapter 3: Suppression of electron thermal conduction by whistler turbulence in a sustained thermal gradient

## 3.1 Heat flux boundary conditions

In the previous chapter we studied the relaxation of heat flux in an ICM-like plasma. Our next step is to look at the long-term nonlinear evolution of the instability with a driving heat flux. Here we model thermal conduction with open boundaries in a magnetized, collisionless plasma by mimicking contact with hot and cold thermal reservoirs. The reservoirs have temperatures $T_h > T_c$ separated by a distance $L_x$, forming a temperature gradient $T' \equiv (T_h - T_c)/L_x$ and driving a heat flux. An initially uniform magnetic field $\mathbf{B_0} = B_0 \hat{\mathbf{x}}$ threads the plasma along the gradient and is free to evolve in time. The initial particle distribution function is chosen to model the free-streaming of particles from each thermal reservoir and has the form

$$f(\mathbf{v}, t = 0) = f_h + f_c = \frac{n_0}{\pi^{3/2}} \left( \frac{e^{-v^2/v_{Th}^2}}{v_{Th}^3} \theta(v_\parallel) + \frac{e^{-[(v_\parallel + v_d)^2 + v_\perp^2]/v_{Tc}^2}}{v_{Tc}^3(1 + erf(v_d/v_{Tc}))} \theta(-v_\parallel) \right) \quad (3.1)$$

where $n_0$ is the initial density, $\theta$ is the Heaviside step function, $v_T = \sqrt{2T/m}$ is the thermal speed, and the parallel and perpendicular directions are with respect to $\mathbf{B_0}$. The cold particles are given a parallel drift speed $v_d$ to ensure zero net
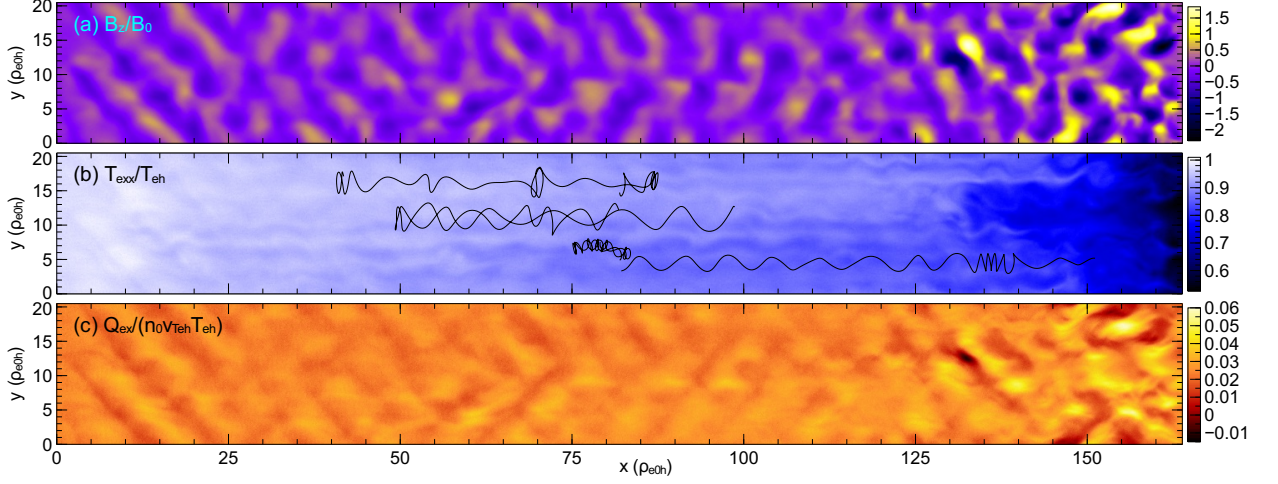
Figure 3.1: Two dimensional plots from the largest simulation ($L_x = 2L_0$) in a saturated state at $t = 800\,\Omega_{e0}^{-1}$. (a) Fluctuations in out-of-plane $B_z$ (b) Temperature $T_{exx}$ with four self-consistent particle trajectories overlaid. (c) Heat flux $q_{ex}$.

current ($\langle v_\parallel \rangle = 0$) in the initial state while the error function $erf(v_d/v_{Tc})$ makes the density of hot and cold particles equal. $f_0$ also has nonzero pressure anisotropy $\left( \langle v_\parallel^2 \rangle \neq \langle v_\perp^2/2 \rangle \right)$ and a heat flux $q_\parallel = \langle v_\parallel v^2 \rangle = q_0$. $f_0$ is not unstable in a 1D system since only off-angle modes resonate with particles near the large phase space discontinuity in $f_0$ at $v_\parallel = 0$.

When particles exit the open boundaries they are re-injected with velocities pulled from $f_h$ (at $x = 0$) or $f_c$ ($x = L_x$). The drift velocity $v_d$ is then recalculated at each time step to ensure that the current of re-injected particles cancels the current of outgoing particles at the cold reservoir. The electromagnetic field components at the thermal reservoir boundaries are $F_y = 0$, $\partial F_x/\partial x = \partial F_z/\partial x = 0$ where $F = (\mathbf{E}, \mathbf{B})$. Periodic boundary conditions are used for both particles and fields in the $y$ direction. In the simulations presented in this chapter, ions in the simulation

37

Table 3.1: Simulation parameters and steady state heat fluxes

| $L_x$ | $\beta_{e0h}$ | $T_{ec}/T_{eh}$ | $q_{ex,f}/(n_0 v_p T_{eh})$ |
|---|---|---|---|
| $L_0 = 82\,\rho_{e0h}$ | 64 | 1/2 | 3.44 |
| $L_0/2$ | 64 | 1/2 | 3.30 |
| $2L_0$ | 64 | 1/2 | 3.26 |
| $L_0$ | 32 | 1/2 | 3.46 |
| $L_0$ | 128 | 1/2 | 3.19 |
| $L_0$ | 64 | 1/4 | 2.56 |

are not evolved in time and act as a charge-neutralizing background.

## 3.2   Simulation Parameters

We have performed six simulations in which $L_x$, $B_0$ and $T_{ec}/T_{eh}$ are varied independently so as to change $T'$ and $\beta_{e0h} = 4\pi n_0 T_{eh}/(B_0^2/2)$. The baseline simulation has $L_x = L_0 = 82\,\rho_{e0h}$, $\beta_{e0h} = 64$, $T_{ec} = T_{eh}/2$, $\omega_{pe}/\Omega_e = 40$, and $T_{eh}/(m_e c^2) = .02$, where $\rho_{e0h} = v_{Teh}/\Omega_{e0}$ is the gyroradius, $\Omega_{e0} = eB_0/(m_e c)$ is the cyclotron frequency, and $\omega_{pe} = (4\pi n_0 e^2/m_e)^{1/2}$ is the plasma frequency. The parameters for each simulation are listed in Table 1. Each simulation uses 560 particles per cell, has a transverse length $L_y$ of 20 $\rho_{e0h}$, and is run to $t = 800\,\Omega_{e0}^{-1}$. The largest simulation ($L_x = 2L_0$) has a spatial domain of 32768 by 4096 grid cells.
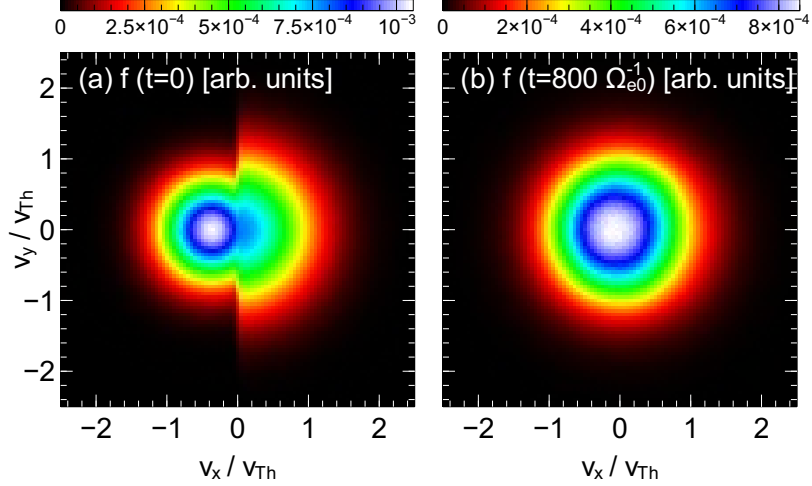
Figure 3.2: Evidence for isotropization of the distribution function by whistler scattering by late time in the center of the simulation domain. (a) $f(t = 0)$ as a function of $v_x$ and $v_y$. (b) $f(t = 800\Omega_{e0}^{-1})$

## 3.3 Whistler Turbulence

Initializing the simulations with $f_0$ leads to an impulse of transient fluctuations in the out-of-plane magnetic field $B_z$ that propagate towards the hot thermal reservoir (evidence for this is shown later). These fluctuations are driven by the initial pressure anisotropy and quickly lead to a sharp drop in the anisotropy to the marginally stable level for firehose-type modes (not shown). The fluctuations rapidly damp, become dynamically unimportant in the simulations, and are not discussed further.

The reinjection and mixing of hot and cold particles results in a continuous source of heat flux in the simulation domain. The heat flux drives off-angle ($k_y \simeq k_x$), slowly propagating ($\omega/k \ll v_{Teh}$), elliptically polarized whistler modes that reach

large amplitude, $\delta B/B_0 \simeq 1$ (fig. 3.1a), and strongly scatter electrons, isotropizing the electron distribution function (Figures 3.2a and b). The heat flux $q_{ex}$ drops well below its initial value $q_{ex0}$. Some reflection of waves occurs at the cold plate boundary but the heat flux is insensitive to the length of the simulation domain, confirming that such reflection does not impact the integrated results.

Strong scattering by the whistlers causes inherently 2D structures to develop in quantities such as the temperature $T_{exx} = m_e \langle v_x^2 \rangle$ (figure 3.1b) and heat flux $q_{ex}$ (figure 3.1c). In figure 3.1b the trajectories of four electron macro-particles from the simulation, tracked starting from an initial position $x = L_x/2$ for a period of 87.5 $\Omega_{e0}^{-1}$ in steady state, are overlaid over $T_{exx}$, which does not vary appreciably during the time of the orbits. Some particles reverse their parallel velocity several times as a result of scattering in the strong magnetic fluctuations. Because the system is 2D the particle out-of-plane canonical momentum, $p_{ez} = m_e v_z - eA_z$, is a conserved quantity. Since $A_z \sim yB_x$ and kinetic energy is mostly conserved in the magnetic fluctuations, the electrons are confined to relatively narrow channels in $y$.

## 3.4   Suppression of Thermal Conduction

Suppression of the heat flux develops over a time of hundreds of $\Omega_{e0}^{-1}$ resulting in a steady state in which a continuous temperature profile has formed between the hot and cold reservoirs (fig. 3.3a) and the heat flux has leveled off to a nearly constant value (fig. 3.3b). Fig. 3.3c shows the time profiles of average heat flux $\langle q_{ex} \rangle_{x,y}$ for six simulations.
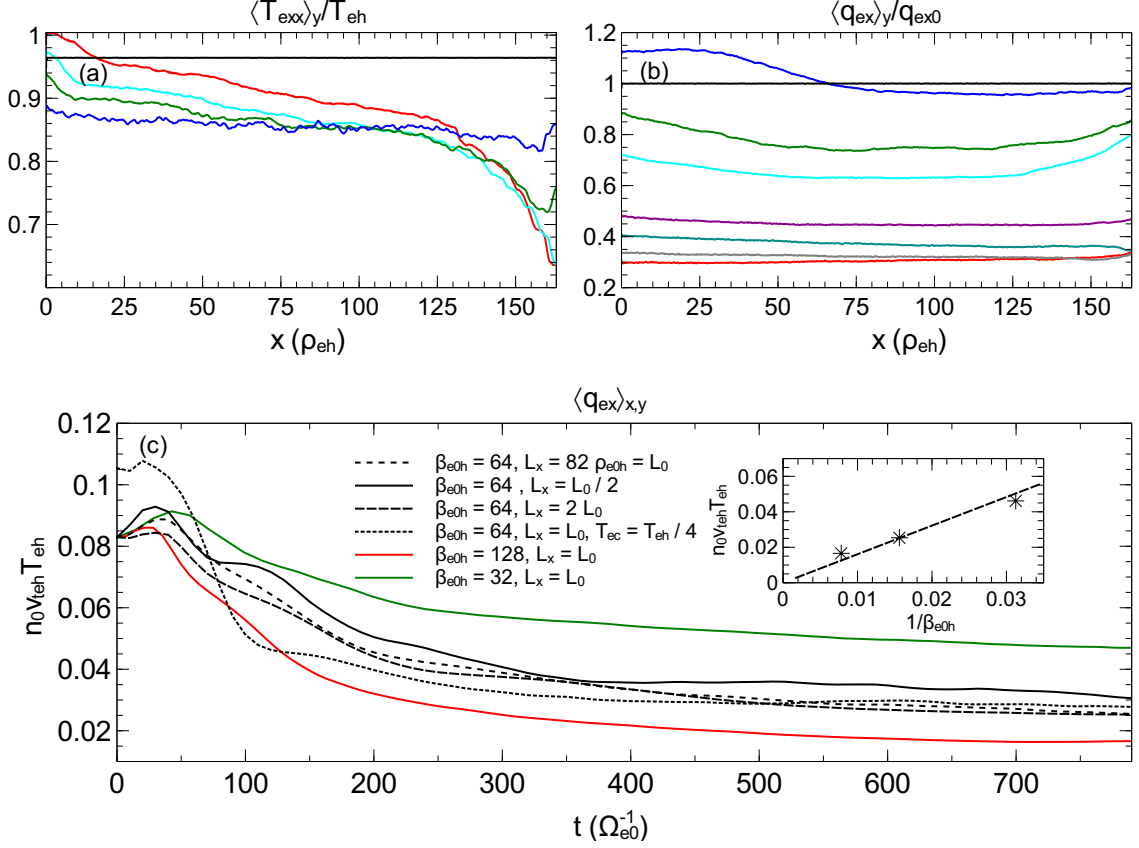
Figure 3.3: Temperature and heat flux profiles. (a) Line plots of $y$-averaged $T_{exx}$ for the run with $L_x = 2L_0$ at times $t\Omega_{e0} = 0$ (black), 80 (blue), 200 (green), 400 (cyan), and 800 (red). (b) Line plots of $y$-averaged heat flux at times $t\Omega_{e0}^{-1} = 0$ (black), 30 (blue), 100 (green), 150 (cyan), 300 (purple), 450 (grey-blue), 600 (grey), and 800 (red). (c) Box-averaged $\langle q_{ex}(t)\rangle_{x,y}$ for the six simulations in Table 1. *Inset*: Linear fit to the steady state heat flux $q_{ex,f}$ as a function of $1/\beta_{e0h}$.

The expectation for a system subject to Coulomb scattering (or another scattering process) is that the heat flux is diffusive, $\mathbf{q}_e \propto -\nabla T_e$. We find instead that the final heat flux is insensitive to the ambient gradient. The black lines in fig. 3.3c correspond to simulations with a fixed $\beta_{e0h} = 64$ but differing box lengths or hot to cold temperature jumps. For all of these runs the heat flux settles at around $0.03\, n_0 T_{eh} v_{Teh}$. Thus, the heat flux rather than the gradient controls the dynamics. As long as $T_{eh}$ is significantly greater than $T_{ec}$, the hot plate controls the final heat flux. However, the three simulations with differing $\beta_{e0h}$ have noticeably different asymptotic heat fluxes that follow the scaling $\langle q_{ex} \rangle_{x,y} \propto 1/\beta_{e0h}$ (fig 3.6c inset). To explain this result we turn to the physics of scattering by large-amplitude whistler waves.

## 3.5   Scattering by whistlers

The physics of resonant interactions of particles with elliptically polarized whistlers, which we again invoke here, was discussed in chapters 1 and 2. In the frame of a single off-angle whistler wave, total kinetic energy is conserved and particles which satisfy the various resonance criteria $v_\parallel = n\Omega_0/k, n = 0, \pm 1, \pm 2, ...,$ are trapped [35]. For $\delta B/B_0 \ll 1$, resonant particles experience small oscillations in the $v_\parallel / v_\perp$ plane. For large-amplitude whistlers ($\delta B/B_0 0.3$) resonances can overlap, leading to irreversible diffusive behavior along circular, constant energy curves in the whistler wave frame [35]. In the presence of multiple whistlers with differing parallel phase speeds some diffusion may also occur perpendicular to circles of constant

energy [35]. Resonance overlap is an effective mechanism for heat flux suppression since it causes large deflections in the particle pitch angle $\phi = \tan^{-1}(v_\perp/v_\parallel)$, quenching the parallel heat flux (as discussed in 2).

To demonstrate that this is the physics at play in our simulations, in fig. 2.3a we show a resonance diagram in $v_\parallel - v_\perp$ for four trapped particles with differing energy in the simulation with $L = 2L_0$ at steady state. Particle energy is mostly conserved and the primary diffusion is in pitch angle [35]. All the particles display significant deflection so the bulk of particles undergo trapping by the whistlers. Also of note is that the nearly-circular contours in velocity space are effectively centered about $v_\parallel = 0$, indicating that the whistler phase speed is small compared to the thermal speed $v_{Teh}$.

To quantify the rate of scattering by the whistlers we calculate the quantity $\langle (x(t) - x(t_0))^2 \rangle$ by averaging over individual trajectories of roughly 8000 particles for the $L_x = 2L_0$ simulation (fig. 3.4b). The diffusion rate $D = \langle v^2 \rangle \tau$ is half the linear slope of $(x - x_0)^2$ at late time, where $\tau$ is the scattering time. We find $\tau \simeq 6.80\,\Omega_{e0}^{-1}$. We plot $x$ versus time for 150 particles in fig. 3.5 to illustrate the particle motion. Some particles are diverted back towards the initial particle location at $y = L_0$ once scattering becomes significant while others maintain their initial direction of propagation. The linear trend of mean-squared displacement in 3.4b is evidence for diffusive behavior. Pitch angle scattering in a spectrum of whistler turbulence was also reported by [43].
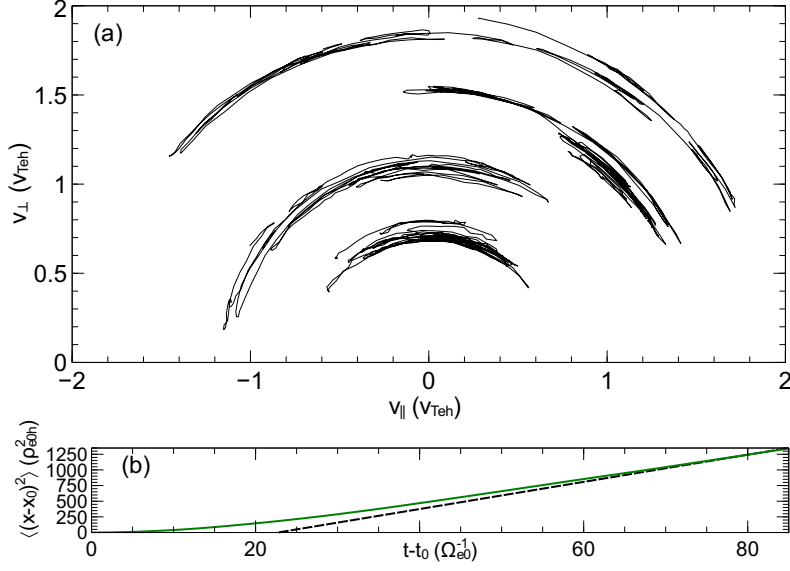
Figure 3.4: Evidence for scattering of electrons by whistlers. (a) Trajectories of particles in $v_\parallel$,$v_\perp$ space showing significant deflection of pitch angle $\phi = \tan^{-1}(v_\perp/v_\parallel)$. (b) Plot of $\langle (x(t) - x(t_0))^2 \rangle$ with linear fit to the slope representing diffusion coefficient $D$.
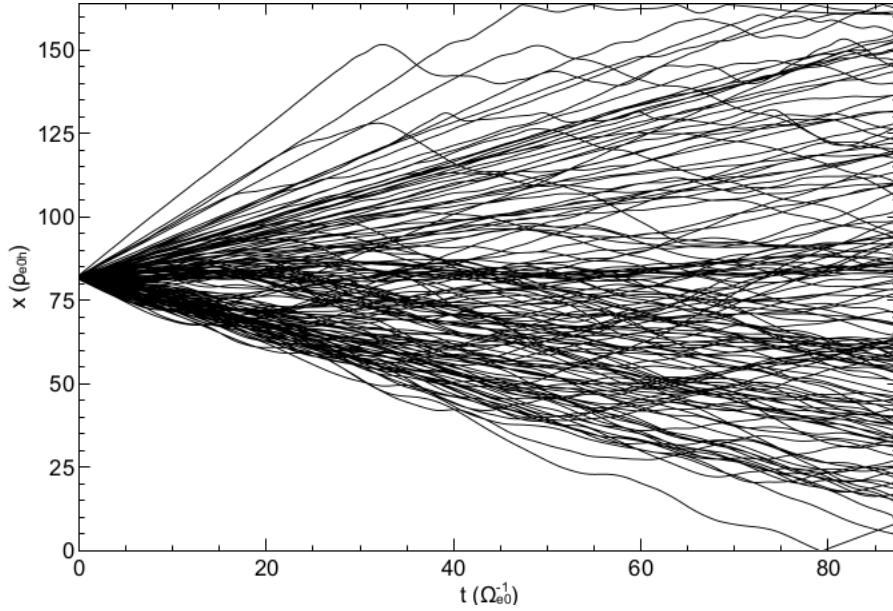


Figure 3.5: Line plots of $x(t)$ for 150 particles in the $L_x = 2L_0$ simulation indicating diffusive behavior.

44

## 3.6 Steady state heat flux

The results of fig. 3.3a have demonstrated that the asymptotic rate of thermal conduction in the presence of large-amplitude whistler waves is largely independent of the temperature gradient and instead follows a scaling $1/\beta_{e0h}$. A simple explanation for this result, consistent with a comment in [27], is that whistlers act as particle scattering centers that propagate at their phase speed $v_p = \omega/k$ and control the net flow of high-energy particles carrying the bulk of the heat flux. The resulting heat flux is simply the product of the phase speed and the thermal energy of the hot plasma, $q_{ex} \sim n_0 v_p T_{eh}$.

The whistler wave phase speed is determined via the cold plasma dispersion relation, $\omega = k^2 \rho_e^2 \Omega_e / \beta_e$. Taking $k\rho_e \sim 1$ (as in section 2.5) for whistlers at high $\beta_e$, we find

$$\frac{\omega}{k} \sim \frac{v_{Te}}{\beta_e}. \tag{3.2}$$

In figure 3.6a we show a spacetime diagram ($t$ versus $x$) of the out-of-plane $B_z$ at a single value of $L_y/2$. After a transient associated with the anisotropy-driven waves of the initial distribution $f_0$ that was discussed earlier, the whistlers propagate at a nearly uniform speed in the direction of $-T'$ ($+\hat{\mathbf{x}}$). To confirm that the unstable modes have $k\rho_e \sim 1$, we show the power spectrum $|B_{k_x}|^2$ for the runs with $L_x = L_0$ at $\beta_{e0h} = 32, 64$ and $128$ in fig. 3.6b. The spectra are nearly isotropic in the 2D Fourier space $k_x - k_y$ (not shown) so in the spectra shown the energy has been summed over $k_y$. We find a spectral index of $-13/3$ for the modes near $k_x \rho_{e0h} = 1$ although we note that the more important point is to establish that the

45
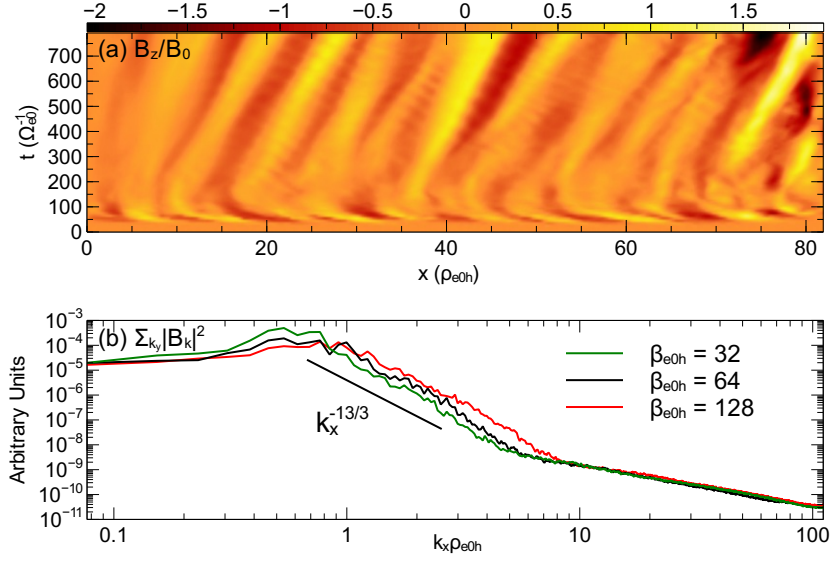
Figure 3.6: (a) Spacetime plot ($t$ versus $x$) of whistler fluctuations propagating through the simulation with $L_x = L_0, \beta_{e0h} = 64$ at $L_y/2$. At early times the initial condition $f_0$ produces fluctuations that reverse direction and are overtaken by the whistlers, which then move to the right. The fluctuations move slowly compared to the thermal speed and most do not reach the cold reservoir at $x = L_0$ by the end of the simulation at $t = 800 \, \Omega_{e0}^{-1}$. (b) Fourier spectra, summed over $k_y$ and plotted as a function of $k_x$ for the simulations with $L_x = L_0$ and $\beta_{e0h} = 32, 64$, and $128$.

spectrum peaks near $k\rho_{e0h} = 1$ even as $\beta_{e0h}$ varies. A more complete exploration of the spectrum requires simulations with a third spatial dimension. In addition we find that for each of the six simulations in Table 1, $q_{ex,f} \simeq 3\,n_0 v_p T_{eh}$, where $v_p$ was measured in the middle of the simulation domain. These results strongly support the scaling

$$q_\parallel = \alpha n_0 \frac{\omega}{k} T_{eh} \sim n_0 m_e \frac{v_{Teh}^3}{\beta_{e0h}} = v_{Teh} \frac{B_0^2}{8\pi}, \qquad (3.3)$$

where $\alpha$ is a coefficient of order unity. Equation (3.3) reveals the crucial role of the background magnetic field in facilitating thermal transport since it controls the propagation of whistlers. In the case of a very small magnetic field the whistlers barely propagate and the thermal conduction is virtually shut off. However, no whistler growth was found in a simulation with $B_0 = 0$ (not shown), indicating that heat flux suppression by whistlers requires a finite ambient magnetic field. Recent PIC simulations with an imposed thermal gradient suggest that pressure anisotropy driven modes are at play when there is no initial ambient magnetic field [44]. Those results are consistent with the transient growth of fluctuations seen in our simulations in the case of $B_0 = 0$. These reach finite amplitude but then rapidly decay on time scales short compared with the development of the heat-flux instability.

## 3.7 Discussion

A caveat of our model is that the imposed thermal gradient is much larger than that measured in environments such as the ICM [27]. However, the present

simulations suggest that the transport is insensitive to the imposed temperature gradient (although the sign of the parallel heat flux is determined by the sign of $-\nabla T_e$ through the whistler phase speed). The point is that heat flux instability is directly driven by the collisionless heat flux, which depends only on the temperature difference across a domain, rather than the ambient gradient. It seems likely, therefore, that the current results apply to cases in which the temperature gradient is far weaker. A full treatment of the ICM also requires the inclusion of weak collisions not present in our kinetic model.

A question is how the microphysics of whistler scattering will affect heating and thermal conduction in the intracluster medium. The scaling of heat flux in (3.3) with $1/\beta_e$ implies a suppression factor of roughly 100 below the free-streaming thermal conduction. The functional dependence $q_\parallel \propto T^{1/2}$ is a noticeable departure from the Spitzer conductivity [16] proportional to $T^{7/2}$ often used in hydrodynamic or MHD models of the ICM (e.g. [45], [46]). Our results may therefore significantly alter the equilibria associated with clusters of galaxies, which result from a balance between thermal conduction and radiative cooling.

Our results show promising similarities with the observations of thermal conduction in the solar wind by Bale et al. [47] in which the heat flux takes on a constant value, independent of collisionality and the ambient temperature gradient, in the weak collisionality regime where the collisional mean-free-path exceeds the temperature scale length. However, much of their data is in a regime of much lower $\beta$ than in the present simulations. In the next chapter we explore the transition from high to low $\beta$ to bring our model in closer alignment with observations.

# Chapter 4:   Wave generation and heat flux suppression in astrophysical plasma systems

The simulations and theory of the previous chapter suggest that the maximum electron thermal conduction parallel to $\mathbf{B}$ scales like $1/\beta$ for $\beta \gg 1$. However, if we had a prescription for lower $\beta$ systems we could try to match results to observations of the solar wind at 1 au, for which we have in-situ measurements of the plasma and electromagnetic fields. This is necessary for our theory to hold any water in the long term. Our result (3.3) is consistent with earlier theoretical models [27–30] and some observations of electron heat flux in the solar wind [48, 49]. As it turns out, the $1/\beta$ limit has recently been confirmed by observations of solar wind heat flux measured by the WIND Spacecraft at 1AU [50] for $\beta \sim 1-6$. However, it is clear from the data shown in [50] that a transition to a different limiting heat flux is at play when $\beta 2$. In the following section we describe a means by which heat flux can be limited at low $\beta$.

## 4.1   Double Layer Heat Flux Suppression

Recent PIC simulation results presented in a series of papers by Li, Drake & Swisdak (hereafter LDS) [51–53] identified a transport suppression mechanism

mediated by electrostatic double layers (DLs) in the $\beta \sim 1$ regime. LDS modeled the outward propagation of a localized source of hot electrons produced at a coronal looptop during a solar flare. In their scheme an initial gradient in the electron temperature drove a parallel electron heat flux. The resulting hot electron current drove a return current carried by the cold background electrons that penetrated into the hot source region. The return current then coupled to the ions via the Buneman instability [54, 55], which in its nonlinear stage of evolution produced a localized electrostatic potential identified as a DL [56–58]. Finite mass (i.e. non-stationary) ions were required in the LDS simulations to capture the interaction between the return current electrons and the ambient ions that led to the formation of the DL.

A DL functions effectively as a mobile parallel-plate capacitor in a plasma, maintaining a potential drop across two layers of opposite charge whose separation is of the order of the Debye length $\lambda_D$ [56]. In the LDS simulations the self-sustaining and long-lived DL (and in some cases multiple DLs, [53]) propagated in the direction of the return current. Heat flux was inhibited as the DLs reflected hot electrons propagating from the source region and continued to accelerate a cold return current opposing the motion of hot electrons. However, suppression of heat flux was modest since only particles with energy less than the DL electrostatic potential were reflected and confined within the source region, while higher-energy hot electrons were allowed to pass through the potential with minimal reduction in energy [51].

LDS's results suggest that DL physics may play a role in magnetized plasmas with sustained temperature gradients but in a more modest $\beta \sim 1$ regime relevant to systems such as the solar wind and coronal looptops, where it has been speculated

that turbulent magnetic fluctuations may be responsible for confining hot electrons during flares [59]. Other systems of interest might include low-luminosity accretion flows and their coronae, since results from GRMHD simulations (e.g. [60]) imply that $\beta$ may be of order unity at high latitudes near the coronae of black holes [61]. We find that DLs indeed play a central role in the $\beta \sim 1$ regime and in the following sections present a series of PIC simulations that reveal the transition from whistler heat flux suppression to suppression by double layers.

## 4.2   Simulation Parameters

We carry out two-dimensional (2D) PIC simulations using the same numerical setup as in chap. 3. In the simulations presented here ion positions and velocities are evolved in time, allowing double layers to form. Ions, with mass ratio $m_i/m_e = 1600$, are initialized with a Maxwellian distribution of temperature $T_{i0} = T_{eh}/2$ and are re-injected into the domain using the above scheme with equal temperatures $T_{ih} = T_{ic} = T_{i0}$.

The simulations scan a range of $\beta_{e0h} = 8\pi n_0 T_{eh}/B_0^2$ from 32 to 1/4 in factors of 2 (32,16,8,...,1/4) using an electron temperature ratio $T_{eh}/T_{ec} = 10$. The simulation domain lengths are $L_x = L_0 = 164 \, d_e$ and $L_y = L_0/2$, where $d_e = c/\omega_{pe}$ is the electron skin depth and $\omega_{pe} = (4\pi n_0 e^2/m_e)^{1/2}$ is the electron plasma frequency. The characteristic velocity of whistlers depends on the wavelength but has an upper limit that scales with the electron Alfvén speed $V_{A,e} = d_e\Omega_{e0}$. However, we normalize electron heat fluxes to the free-streaming value $q_0 = n_0 v_{T_{eh}} T_{eh}$ as in 3.

Since DLs are generated near the cold reservoir and propagate towards the hot thermal reservoir at $x = 0$, we stop the simulation before the DL conduction front reaches the hot boundary and significantly impacts plasma injection. For $\beta_{e0h} = 1$ this corresponds to a time of $t\Omega_{e0} \sim 7200$. Other parameters in the simulations are $\omega_{pe}/\Omega_{e0} = 5\sqrt{\beta_{e0h}}$, and $T_{eh}/(m_e c^2) = 0.02$, which sets $v_{Th}/c = 1/5$ such that electrons are mostly non-relativistic. Each simulation uses 560 particles per species per cell and has a grid of 4096 by 2048 cells.

## 4.3 Simulation Results

## 4.4 Whistler regime

Figure 4.1 contrasts the dynamics of the $\beta_{e0h} = 1$ [(a)-(e)] and 16 [(f)-(j)] simulations. In the case of $\beta_{e0h} = 16$ the results are similar to the large $\beta_e$ (32, 64, and 128) runs of chap. 3. Strong heat flux suppression below the free-streaming value takes place throughout the simulation domain [Fig. 4.1(f)] and is associated with scattering of electrons by large-amplitude oblique whistler fluctuations $\delta B/B_0 \sim 1$ in the out-of-plane $B_z$ in 4.1(g).

Figure 4.1(j) shows substantial heating of ions, correlated with the turbulent whistler fields near the cold reservoir at $x = L_x$. In some locations the peak ion temperature is 40% larger than $T_{i0}$. The ions are scattered by the spatially localized, $\rho_{e0h}(= \sqrt{\beta_{e0h}}d_e)$ scale whistler electric fields and have an unmagnetized response to the turbulence ($\rho_{i0} \gg \rho_{e0h}$). The electric field fluctuations $E_x$ associated with these whistlers are shown in Fig. 4.1(h). To estimate the rate of ion heating we calculate
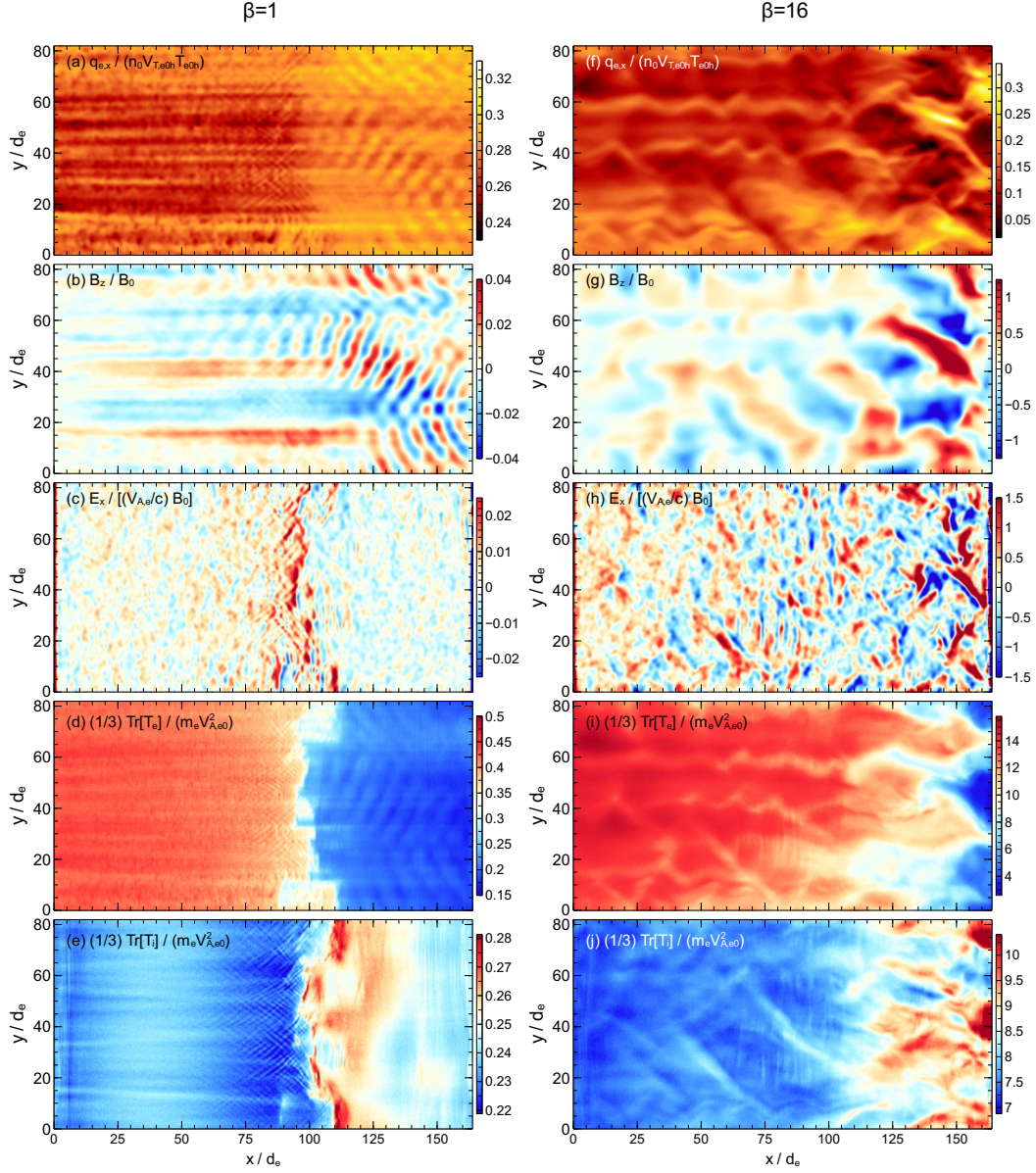
Figure 4.1: 2D plots from the $\beta_{e0h} = 1$ [(a)-(e)] and 16 [(f)-(j)] simulations at $t\Omega_{e0} = 3640$ and 910, respecively. (a) Suppression of $q_{ex}$ by DLs located between $x/d_e \sim 85-115$ that propagate towards the hot reservoir at $x = 0$. (b) Out-of-plane $B_z$ showing elongated magnetic structures mostly to the left of the DLs and oblique whistlers mostly to the right of the DLs. (c) Parallel electric field $E_x$ showing a DL conduction front (bright red spots). (d) One third of the trace of the electron temperature tensor $T_e$. (e) Same as (d) but for ions showing substantial heating to the right of the DLs. (f) Strong suppression of $q_{ex}$ by whistlers. (g) Large-amplitude whistler fluctuations in $B_z$. (h) Parallel whistler electric fields in $E_x$ (near the cold reservoir at $x = L_x$) and turbulence associated with a small DL conduction front near $x = L_x/2$. (i) 2D structure of $T_e$ in whistler fields. (j) Heating of ions by whistlers.

an energy diffusion coefficient for homogeneous whistler turbulence

$$D_W = \frac{\langle \Delta v_i^2 \rangle}{t} = \frac{q_i^2}{m_i^2} \int_0^\infty d\tau \langle \delta E_x(0) \delta E_x(\tau) \rangle. \tag{4.1}$$

Similar expressions for electron diffusion in whistler turbulence are given in [43]. The dynamics of (4.1) can also be framed as a resonant diffusive process which is essentially Landau damping [see e.g. [62] and [63]]. Assuming isotropic turbulence and dropping factors of order unity we get $D_W \sim (q_i^2/m_i^2)\tau_c \langle \delta E^2 \rangle$, where $\tau_c$ is the correlation time of the electric field, which we take to be $\tau_c = \rho_{e0h}/v_p \sim \beta_{e0h}/\Omega_{e0}$.

The electric field fluctuations $E_x$ [Fig. 4.1(h)] are of the order of $(V_{A,e}/c)\, B_0$, a factor of $\sqrt{\beta_{e0h}} = 4$ larger than the electric field of a parallel propagating whistler with phase speed $v_p = v_{Teh}/\beta_{e0h}$,

$$\delta E = \frac{v_p}{c}\delta B \sim \frac{v_{Teh}}{c\beta_{e0h}}B_0. \tag{4.2}$$

However, we still measure phase speeds of the order $v_{Teh}/\beta_{e0h}$ in the $\beta_{e0h} = 16$ simulation (not shown). The crux is that these whistlers are oblique, with $\mathbf{k}$ nearly parallel to $\delta\mathbf{E}$. To be consistent with Faraday's Law, $\mathbf{k} \times \delta\mathbf{E} = (\omega/c)\delta\mathbf{B}$, the electric field is enhanced by a factor of $1/\sin(\theta)$ relative to (4.2), where $\theta$ is the angle between $\mathbf{k}$ and $\delta\mathbf{E}$. We nonetheless take expression (4.2) to be correct and use it as a reasonable lower bound for $\delta E$ in the large-amplitude and high-$\beta$ regime.

Using (4.2) leads to $D_W \sim B_0^2/(4\pi n_0 m_i)\, \Omega_{i0}$. Multiplying by $(1/2)n_0 m_i$ we arrive at an ion heating rate

$$\frac{\partial W_i}{\partial t} = \frac{1}{2}n_0 m_i D_W \sim \frac{B_0^2}{8\pi}\Omega_{i0}. \tag{4.3}$$

Inserting numbers from the $\beta_{e0h} = 16$ simulation (4.3) yields a net heating of roughly

10% of $T_{i0}$ by $t\Omega_{e0} = 910$. Spatially averaging $(1/3)Tr[T_i]$ over all $y$ and the region $x = 0.7\,L_x$ to $x = 0.9\,L_x$ (where large-amplitude whistlers are most prevalent) yields ion heating of around 5% of $T_{i0}$, which is within a factor of 2 of the analytic estimate. Equation (4.3) suggests local ion heating can occur on the very rapid time scale of ion cyclotron motion in the high-$\beta$ ICM when strong whistler turbulence is present. Over long time scales in the ICM the damping of the whistlers associated with ion heating can be offset by a net positive growth rate from the heat flux instability. In the regime of large collisionless heat flux the damping from ions does not significantly impact whistler stability (see Fig. 4.4 and section 4.9 as well as [37]). The regime of smaller heat fluxes and marginal heat flux instability will be investigated in future work.

## 4.5   DL regime

In the $\beta_{e0h} = 1$ simulation a thermal conduction front, containing several DLs (as in [53]) in fig. 4.1(c), divides the simulation domain into "hot" $(x/d_e 100)$ and " cold" $(x/d_e 100)$ regions. The conduction front originates near the cold thermal reservoir and propagates into the hot region (evidence for this is shown in figure 2). The DLs are the dark-red, mostly vertical structures in fig. 4.1(c) around $x/d_e = 100$ and have parallel wavelengths of roughly $10\,\lambda_{Deh}$ [51], where $\lambda_{Deh} = V_{Teh}/(\sqrt{2}\omega_{pe})$ is the hot electron Debye length. These wavelengths are consistent with the unstable modes of the Buneman instability [54]. Two DLs are present at the bottom of figure 4.1(c) around $y/d_e = 5$ and $x/d_e \sim 87$ and $x/d_e \sim 110$ [53]. The potential jump across the DL front is $e\Phi_{DL} \sim 0.4\,T_{e0h}$, consistent with the results and analytic

predictions of [52].

The DLs are dynamical structures that tend to break up and reform over time, developing nontrivial structure in the perpendicular ($y$) direction. The perpendicular length scale for the DLs is roughly $30\,\lambda_{Deh}$, consistent with results from previous 2D PIC simulations of double layers (e.g. [64, 65]), although the mechanism that sets the angle between the DL electric field and $B_0$ (and hence $k_\perp/k_\parallel$) remains an open question [66], which we do not address in this paper.

Heat flux suppression for $\beta_{e0h} = 1$ [fig. 4.1(a)] is moderate, with a minimum heat flux of roughly $0.24\,q_0$ in the hot region. Mostly rightward-propagating oblique whistlers ($kd_e \sim 1$) with small saturation amplitude ($\delta B/B_0 \sim 0.04$) are present in the cold region, while the hot region contains no whistlers and instead develops elongated magnetic structures $B_z$ with $k_\perp d_e \sim 1$ and $k_\parallel d_e \sim 0.07$ [fig. 4.1(b)]. Note the reversals in the sign of $B_z$ along the $y$ direction. These structures seem to merge with the whistler fluctuations at the approximate location of the conduction front at $x/d_e \sim 100$ and are discussed in more detail in section 4.10.

The elongated magnetic structures do not appear to significantly impact the heat flux [fig. 4.1(a)], which is nonetheless modulated by thin streams with even smaller perpendicular wavelength in the hot region. Rather, it is the DLs, which reflect hot electrons and accelerate the return current, that reduce the overall heat flux in the hot region. Evidence for reflected hot particles and the return current are shown in figure 3. The small-amplitude whistlers in the cold region have a negligible impact on the heat flux (4.1a) unlike in the high $\beta_e$ regime.

Figure 4.1(d) shows the trace of the electron temperature tensor in $(x, y)$,

indicating a sharp discontinuity in $T_e$ around the conduction front at $x/d_e \sim 100$ with temperatures somewhat less than $T_{e0h}$ at the hot reservoir and $T_{e0h}/3$ at the cold reservoir ($T_{e0h} = 0.5\,m_e V_{A,e0}^2$). The ion temperature [fig. 4.1(e)] reveals local heating to be roughly 12% above the injection temperature $T_{i0}$ (note that $T_{i0} = 0.25 m_e V_{A,e0}^2$).

A simple estimate for ion heating by the DL front can be obtained by calculating the change in kinetic energy of ions accelerated by the DL. We assume ions are initially cold and that they gain a velocity $v_\Phi = \sqrt{2e\Phi_{DL}/m_i}$ as they cross the DL in the $+\hat{x}$ direction (the velocity of the DL is small compared with $v_\Phi$). The result is a distribution with two beam-like populations (one with $v_x = 0$ and the other with $v_x = v_\Phi$) in the cold region. The effective thermal energy of the ions is $(3/2)\Delta T_i = (1/2)m_i v_\Phi^2/4$. With $e\Phi_{DL} \sim (2/5)T_{eh}$, we find

$$\Delta T_i \sim \frac{1}{15}T_{eh}, \tag{4.4}$$

which predicts a heating of about 12% above $T_{i0}$, close to the observed heating in fig. 4.1(e).

## 4.6 Generation and propagation of the DLs

Figure 4.2 shows a spacetime diagram of the electric field $E_x$, at a cut along $y = L_y/2$ for the $\beta_e = 1/4$ [4.2(a)], 1 [4.2(b)], and 16 [4.2(c)] simulations. At early times the initial electron distribution function $f_0$ (3.1) relaxes, generating short-wavelength ($k\lambda_{Deh} \sim 1$), large-amplitude electron acoustic waves resulting from two-stream instability between the hot and cold electron populations [67], visible for all $x$ near $t = 0$. These waves damp out early on in the simulation and do not impact the subsequent dynamics. Also present at early times are plasma waves (purple lines
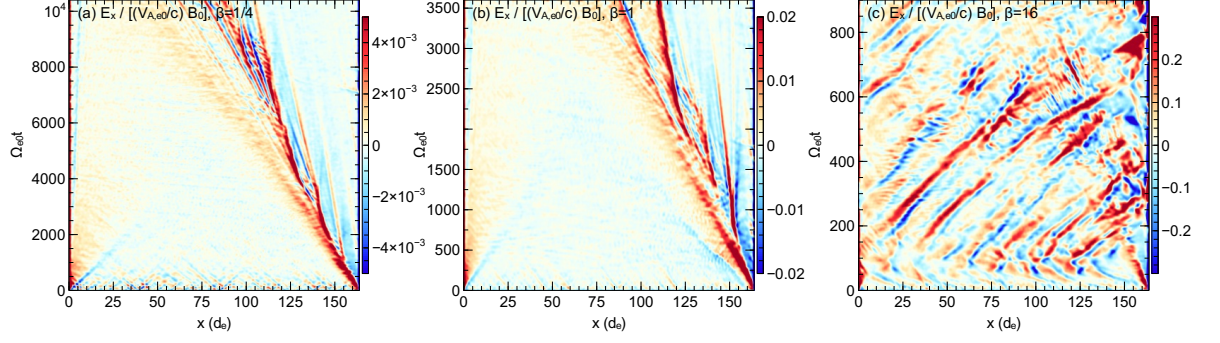
Figure 4.2: Spacetime diagrams of $E_x$ at $y = 3.2\,d_e$ for three values of $\beta_{e0h}$ showing DL formation at the cold reservoir $x = L_0$. (a) $\beta_{e0h} = 1/4$: several strong DLs form and travel towards the hot reservoir, emitting slow-moving ion-acoustic shocks to the right. (b) $\beta_{e0h} = 1$: Similar to (a) but with two primary DLs forming at later stages of the simulation. (c) $\beta_{e0h} = 16$: $E_x$ is dominated by rightward-traveling whistler fluctuations that overtake the weak DL.

merging with the electron acoustic modes) which propagate from the cold region to the hot region and have $kd_e \sim 3$. While these waves are fully resolved in time in the simulation, data outputs are less frequent and show a strongly alternating pattern. These waves tend to damp out by the middle of each simulation while confined to the region to the left of the DL.

In 4.2(a-c) a DL forms at early times near the cold reservoir at $x = L_x$ and then propagates toward the hot reservoir at roughly the acoustic speed $V_s \sim \sqrt{(T_{e0h} + T_{i0})/m_i}$ [52]. A single DL can be distinguished in the electric field $E_x$ by a large positive amplitude on its leading edge to the left, followed by a small negative leg on the right [51–53]. Each DL grows in amplitude as it is continually fed by return currents but stabilizes itself by emitting an ion acoustic shock towards the cold reservoir, which can be identified by the nearly vertical straight lines with positive amplitude (red) to the right of the DLs in fig. 4.2 [52,53]. The shocks quench DL growth by reflecting cold return current electrons before they reach the DLs [52,53].

However, the shocks damp over time [see equation (4.4)], leading to subsequent DL growth and shock re-emission.

Increasing $\beta_{e0h}$ reduces the number and robustness of the DLs [several are visible in fig. 4.2(a), two in 4.2(b) and one only at early time in 4.2(c)]. Increasing $\beta_{e0h}$ also increases the strength of whistlers. For $\beta_{e0h} = 16$ [4.2(c)] the DL front is essentially overwhelmed by whistler electric fields (seen as rightward propagating lines in the whole domain for $t\Omega_{e0}100$)) as the waves propagate toward the hot reservoir. The weakness of the DLs in the high $\beta_e$ regime is a result of strong scattering of return current electrons by whistlers (not shown), which removes the drive mechanism for Buneman instability and hence suppresses DL formation and propagation.

## 4.7   Electron dynamics in the hot and cold regions

The electron distribution function for lower $\beta_{e0h}$ is similar to $f_0$ in Eq. (3.1) but has been altered by the DL potential. Figures 4.3(a) and (b) show color plots of $f_e(v_x, v_y)$ in the $\beta_{e0h} = 1$ simulation at $t\Omega_{e0} = 3640$, averaged over spatial regions to the left (hot region) and right (cold region) of the DL indicated by vertical white lines in fig. 4.3(c). The contours of $\ln(f_e)$ are overlaid in green. In fig. 4.3(a) an accelerated return current beam (the bright spot to the left of $v_x = 0$) is present while the contours indicate that the distribution function is smooth and roughly circular for $v_x > 0$. The discontinuity (i.e. hot/cold interface) in the distribution of injected electrons $f_0$ at $v_x = 0$ has been filled in by hot particles with $-\sqrt{2e\Phi_\Phi/m_e}v_x0$ reflected by the DL potential. In figure 4.3(b) the hot/cold interface is shifted
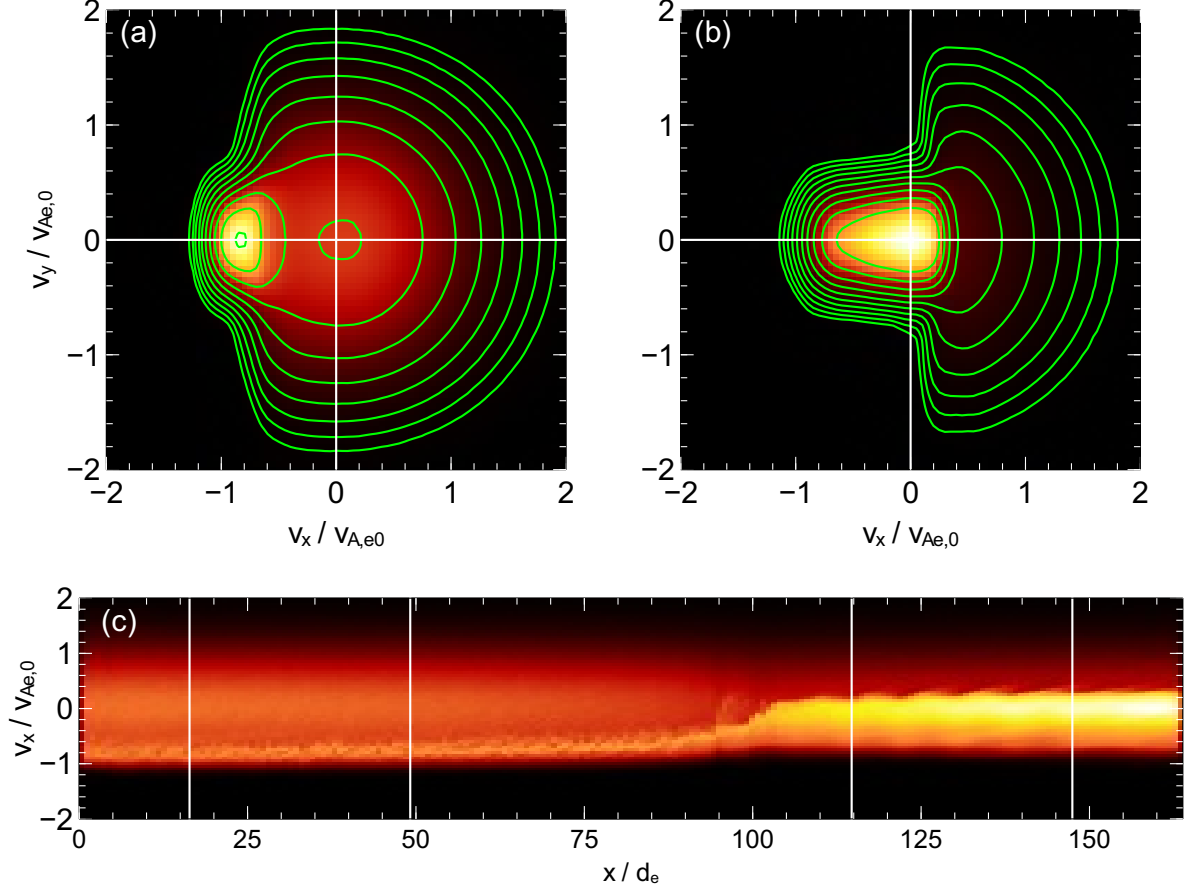
Figure 4.3: Plots from the $\beta_{e0h} = 1$ simulation taken at $t\Omega_{e0}^{-1} = 3640$. (a) Electron distribution function $f_e$ (background color) and $\ln(f_e)$ (green contours) in $v_x - v_y$ space averaged over the spatial region $x = 0.1\,L_x$ to $x = 0.3\,L_x$ (the "hot" region) and all $y$. (b) Same as (a) but averaged over $x = 0.7$ to $0.9\,L_x$ ("cold" region). (c) $f_e$ in the phase space $x - v_x$ averaged over a thin strip in $y$ near $y = L_y/2$. The sections in $x$ over which $f_e$ was averaged to produce (a) and (b) are indicated by vertical white stripes.

slightly to the right but remains near $v_x = 0$. Figure 4.3(c) shows the phase space

profile $f_e(x, v_x)$ of electrons averaged over a thin vertical extent in $y$ near $y = L_y/2$.

The presence of return currents is evident for all $x$, which focus into a narrow beam

for $x/d_e 100$. The narrowing of the overall width in $v_x$ from hot to cold regions

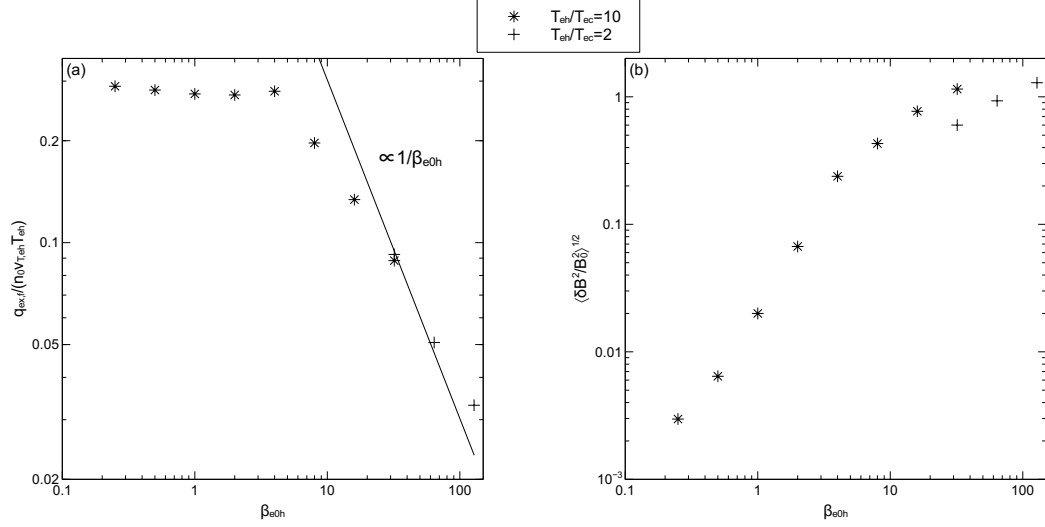reveals the gradient in the electron temperature shown in figure 4.1(d).

Figure 4.4: (a) Plot of the final measured heat flux from simulations as a function of $\beta_{e0h}$, normalized to the free-streaming value $q_{e0} = n_0 v_{Teh} T_{eh}$. Data from fig. 3.4 is shown as plus signs while new simulation data is shown in asterisks. A line proportional to $1/\beta_{e0h}$ (as in fig. 3.3c) is overlaid. (b) Late-time perturbed magnetic field amplitudes $\langle \delta B^2/B_0^2 \rangle^{1/2}$ as a function of $\beta_{e0h}$, obtained by averaging over $x = 0.7\,L_x$ to $x = 0.9\,L_x$ and all of $y$. The extent in $x$ was chosen to always be to the right of the DL conduction front for the new simulations with mobile ions.

## 4.8   Electron thermal conduction

Figure 4.4(a) shows the late time electron heat flux as a function of $\beta_{e0h}$, including the new simulations with $T_{eh}/T_{ec} = 10$ and mobile ions as well as the inset data from fig. 3.4 (with $T_{eh}/T_{ec} = 2$ and stationary ions). The $1/\beta_{e0h}$ scaling (shown as a solid line overlaid) matches the data for $\beta_{e0h} 16$. Since the data at $\beta_{e0h} = 32$ with and without mobile essentially overlaps, we confirm that the ions have little impact on the heat flux at high $\beta_{e0h}$. A rollover to a roughly constant value $q/q_0 \sim .29$ in the final heat flux occurs for $\beta_{e0h} \leq 4$ and is set by the DL potential as shown by the following calculation. Assuming $e\Phi_{DL}/T_{eh} = 0.4$, that return current electrons are a $T = 0$ beam with velocity $v_b/V_{Teh} = -0.8$ [from fig. 4.3(a)], that hot electrons

with $|v_\parallel| \leq \sqrt{2e\Phi/m_e}$ contribute no current or heat flux owing to reflection by the DL, and imposing zero net current we calculate the heat flux in the hot region to be $q_{ex}/n_0 V_{Teh} T_{eh} \sim 0.33$, which is close to the measured value of 0.29.

## 4.9  Saturated whistler amplitudes

We document the strength of the whistler heat flux instability over the range of our high $\beta_{e0h}$ simulations, by showing in figure 4.4(b) the spatial average of the perturbed magnetic field, $\langle \delta B^2/B_0^2 \rangle^{1/2}$. The data from each simulation is from late time such that the turbulence has saturated. In simulations with DLs, the DL front has propagated into the center of the simulation domain. The spatial region for averaging is $x = 0.7\, L_x$ to $x = 0.9\, L_x$ and all of $y$. For the high $\beta_{e0h}$ runs this is where the whistler turbulence is strongest and for the low $\beta_{e0h}$ runs with DLs it is the "cold" region. The general trend in figure 4.4(b) is increasing magnetic fluctuation amplitude as $\beta_{e0h}$ is increased. Two distinct regimes are evident in this figure 4.4(b): the region of strong heat flux instability ($\beta_{e0h}4$), where the characteristic saturated whistler amplitude approaches $B_0$ as $\beta_{e0h}$ is increased; and the region of weak (or nonexistent) heat flux instability for $\beta_{e0h}1$, where the magnetic fluctuations mostly consist of the elongated structures mentioned in section 4.5. We now review the basic physics of heat flux instability and describe these two regimes.

## 4.9.1  Strong heat flux instability

In the high-$\beta_{e0h}$ regime the oblique whistler goes to long wavelengths, $k\rho_e \sim 1$, and the Landau resonance at $v_x = v_p \sim v_{Te}/\beta_{e0h} \ll v_{Teh}$ aligns with the hot/cold

interface in $f_e$ (3.1). Once amplitudes (and hence nonlinear trapping widths) are large enough, the Landau and cyclotron resonances can simultaneously overlap (see fig. 2.4), allowing whistler turbulence to isotropize the hot electron distribution function about the characteristic whistler phase speed. As the hot electrons are scattered about $v_p$ they continue to release free energy and drive whistler growth. To estimate the whistler saturation amplitude in this regime, we calculate the free energy difference $\Delta W = W_{h,final} - W_{h,initial}$, between the final, isotropized distribution and an initial half-Maxwellian distribution of hot electrons moving with $v_x > 0$. The details of the calculation are shown in Appendix A.

To maintain zero net current in the final state, cold return current electrons must also be displaced in the $v_x - v_y$ plane to cancel the current $\sim v_p$ of the isotropized hot particles. In these simulations the return current drift is reduced by re-injection at the cold thermal reservoir as the current of hot particles is suppressed by whistler scattering. We therefore neglect the energetics of cold return current electrons in this calculation, noting that in general an induced electric field could also maintain current neutrality [27, 32, 37].

We find that, to lowest order in $v_p/v_{Teh}$, the energy lost by the hot electron half-Maxwellian as it scattered is proportional to $v_p/v_{Teh}$ (??). For a linear whistler wave at high $\beta$, the energy content is mostly in magnetic field fluctuations and particle kinetic energy and electric fields can be neglected. This should hold true for large-amplitude whistlers as well. Taking $\Delta W \sim -n_0 T_{e0h} v_p/v_{Teh}$ with $v_p = v_{Teh}/\beta_{e0h}$ and
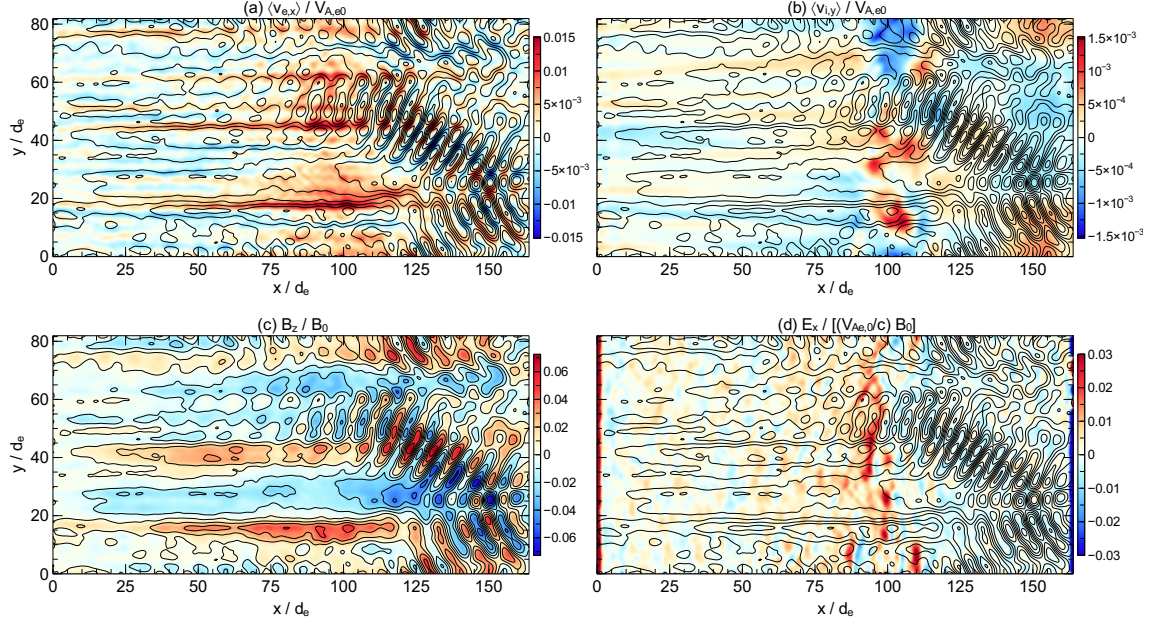
Figure 4.5: 2D plots showing the presence of whistlers and elongated magnetic structures at $t\Omega_{e0} = 3640$ in the $\beta_{e0h} = 1$ simulation. The schematic for current closure, producing the elongated magnetic structures seen for $x/d_e 100$, is described in the text. Each plot has contours of out-of-plane $B_z$, representing in-plane current, overlaid. (a) Average parallel electron velocity $v_{ex}$. (b) Average perpendicular ion velocity $v_{iy}$. (c) $B_z$. (d) $E_x$.

$\beta_{e0h} = 8\pi n_0 T_{eh}/(B_0^2)$, we obtain

$$W_{whistler} \sim \frac{\langle \delta B^2 \rangle}{8\pi} \sim \Delta W_h \sim \frac{B_0^2}{8\pi}, \tag{4.5}$$

i.e., $\delta B \sim B_0$. This explains why there seems to be an order unity $(B_0)$ limit on the

size of magnetic fluctuations in the simulations in fig. 4.4(b). The limit comes from

free energy constraints on the hot electron distribution function as it is scattered

by the large-amplitude whistlers. Coincidentally the $\delta B \sim B_0$ at high $\beta$ result was

also predicted in [37] through a resonance broadening estimate.

## 4.9.2 Weak heat flux instability

In the $\beta_{e0h}1$ regime two factors lead to the stabilization of oblique whistlers: the phase speed of the whistlers and the impact of the DL on the electron distribution functions. Since the characteristic phase speed of the whistlers is the electron Alfvén speed $V_{A,e}$, in the low $\beta_{e0h}$ regime the phase speed exceeds the hot thermal speed. Since the hot/cold interface remains near $v_x = 0$, only very long wavelength whistlers ($kd_e \ll 1$) could potentially resonate with electrons near the interface. Such long wavelength modes are not seen in our simulations. Thus, at low $\beta_{e0h}$ the whistler Landau resonance is at the wrong location in velocity space. The DL front also modifies the electron distribution in the vicinity of $v_x = 0$ in both the hot and cold regions so as to enhance the stability of whistlers in this regime. Hot particles reflected by the DL move the hot/cold interface to the left in the hot region [fig. 4.3(a)] so the Landau resonance is stabilizing. In figure 4.3(b), on the other hand, the discontinuity in $f_e$ remains near $v_x = 0$ but for whistlers with $kd_e \sim 1$ the Landau resonance again lies in the region $v_x > v_{Teh}$, well away from the location of the discontinuity.

## 4.10   Kinetic Alfvén Wave-like Structures

The dynamics of the elongated magnetic structures in $B_z$ in the $\beta_{e0h} \leq 1$ simulations can be described in terms of current loops formed in the $x, y$ plane. In figure 4.5 we present the components of these current loops in the $x, y$ plane ($v_{ex}$, $v_{iy}$ as well as $B_z$ and $E_x$). The region enclosed by these loops contains an out-of-plane $B_z$ [fig. 4.5(c)]. Each plot in figure 4.5 has contours of $B_z$ overlaid,
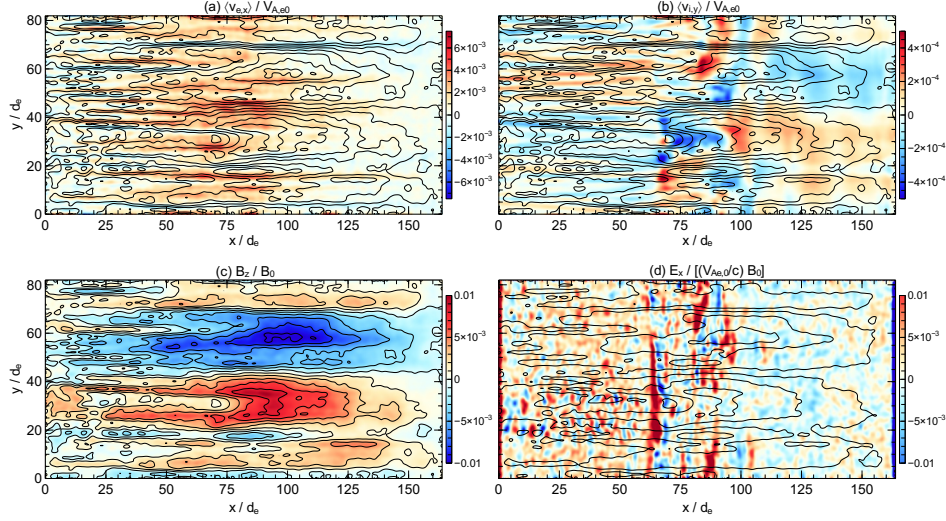
Figure 4.6: Same as figure 4.5 but for the $\beta_{e0h} = 1/4$ simulation at $t\Omega_{e0} = 1820$.

which correspond to the streamlines of the in-plane current, which can be written

as $\mathbf{J}_{in-plane} \propto \hat{z} \times \nabla B_z$. We illustrate the nature of the structures by focusing on

the oblate red structure in fig. 4.5(c) roughly centered around $y/d_e = 40$ in the hot

region to the left of the DLs [seen in $E_x$, fig. 4.5(d)]. The upper and lower sections of

current that produce this particular structure result from electrons streaming along

$\mathbf{B_0} = B_0\hat{x}$, seen in fig. 4.5(a) as red ($y/d_e \sim 45$) and blue ($y/d_e \sim 36$) stripes in

$\langle v_{ex} \rangle$ that closely follow the contours of in-plane current. Note that the electron

current $J_{ex} = -en_e\langle v_{ex} \rangle$ differs in sign from $\langle v_{ex} \rangle$. The current is closed in the y

direction by ions, which in fig. 4.5(b) show a negative (blue) flow $\langle v_{iy} \rangle$ centered

around $x/d_e \sim 18$ and a positive (red) flow near $x/d_e \sim 90$. In addition, oblique

whistlers in the cold region to the right of the DLs may play some role in closing

currents near the DLs. While the closure of in-plane currents by electrons and ions

is typical of kinetic Alfvén waves (KAWs) [68, 69], $k_\perp \rho_i = \sqrt{m_i/m_e} k_\perp \rho_e$ is large

so that the ions behave as unmagnetized particles in response to these disturbances

(similar to ion heating by whistlers, section 4.4). The waves therefore differ from the standard magnetized ion treatment of KAWs. Figure 4.6 shows the same quantities as figure 4.5, but for the $\beta_{e0h} = 1/4$ simulation, in which no whistler turbulence is present.

The perpendicular wavelength $k_y$ of the elongated structures is closely linked to the variation in the $y$ direction of the DL electrostatic potential $\Phi_{DL}$ (see $E_x$ in 4.5(d)). We conjecture that it is the $y$ dependence (see 4.5) which causes return currents in the entire simulation domain to vary in $y$ and produces the elongated structures, but leave a more detailed exploration of the generation mechanism to future work.

## 4.11   Discussion

Using 2-D particle-in-cell simulations we have explored the physics of magnetized collisionless plasmas with a large, imposed electron heat flux for a range of $\beta_e$ from 1/4 to 32. The primary result is that a transition from heat flux suppression by whistler waves at high $\beta$ to that of electrostatic double layers (DLs) at low $\beta$ occurs [figure 4.4(a)]. In this transition the whistler scaling for the parallel heat flux, $q_e/q_0 \sim v_{Te}/\beta_e$, rolls over to a constant value $q_e/q_0 \sim 0.3$ for the DL regime, where $q_0 = n_0 v_{Te} T_e$ is the free-streaming collisionless heat flux. This result could be compared with in-situ measurements of the solar wind heat flux at 1 AU (e.g. [50]).

The formation of the DLs comes about as a result of coupling between ions and electrons, which was not included in the previous chapter's numerical model (3.1) [see also [37]]. The assumption of infinite mass ions in these models was nonetheless

justifiable since DL formation is suppressed at high $\beta$ and ion damping has a small effect on the stability of whistlers. The DLs are generated by a return current linked to the strong imposed electron heat flux [51–53]. The DL system is inherently non-steady since the DL front propagates at finite speed against the direction of heat flux and periodically emits shocklets. Ion-electron coupling also includes ion heating downstream of the DLs at low $\beta$ and resonant heating of ions by whistlers at high $\beta_{e0h}$.

The heat-flux-driven whistlers saturate at large amplitude $\delta B \sim B_0$ in the high-$\beta$ regime and are suppressed at low $\beta$. The dominant magnetic perturbation at low $\beta$ was found to be an electron scale $k_\perp d_e \sim 1 \gg k_\parallel d_e$ mode with characteristics similar to a kinetic Alfvén wave. While the detailed generation mechanism for this mode has yet to be explored, we suspect it results from the inherent two-dimensionality of the DL conduction front and its associated electrostatic potential. This mode does not appear to impact electron thermal conduction but may be observable in $\beta 1$ astrophysical plasmas such as the solar wind. Future measurements of heat fluxes and electromagnetic fields in the solar corona from the Parker Solar Probe mission could also be compared with our results.

A caveat of our model is that the simulation domain contains far fewer electron skin depths $d_e$ than than of a real astrophysical system. As a result, the imposed thermal gradient is much larger than that typically inferred in astrophysical environments such as the ICM [27]. On the other hand, our results on the limiting heat flux are surprisingly insensitive to the temperature gradient imposed in our simulations. Further, observations in the solar wind have confirmed the $1/\beta$ scaling

of the limiting heat flux [50] in spite of the fact that the gradient scale length of the temperature in the solar wind is very large compared with all kinetic scale lengths. The consequences of larger system sizes and weaker thermal gradients, e.g. the impact on saturation of and scattering by whistler fluctuations, are presently being explored. We also note that Coulomb collisions are not included in our model. The transition between the heat flux in systems with short collisional mean-free-paths and that of collisionless systems remains to be explored. Future work will address the impact of these results in fluid models of astrophysical plasmas.

## Chapter 5:   Conclusion

## 5.1   Summary

In this thesis we explored the physics of thermal conduction in weakly magne-tized, weakly collisional plasmas such as the intracluster medium of galaxy clusters. Our tools were (mostly) 2D particle-in-cell (PIC) simulations and a combination of linear and nonlinear analytic theory. We found that the whistler wave, a high-frequency extension of the MHD fast mode, can substantially reduce transport of heat in such plasmas when a large heat flux is imposed on the system. The spatial scale of the whistler in this case is roughly the electron Larmor radius. The physics of the transport reduction is linked to wave-particle resonances between electrons and the self-consistently generated whistler waves. The result is that the maximum allowed thermal flux in ICM-like plasmas appears to scale like $1/\beta$, which can be a severe constraint since $\beta \sim 100$ in the ICM. This result seems to further discourage the idea that thermal conduction could prevent cooling catastrophe in the dense, cool cores of some galaxy clusters.

Since the current spatial resolution of the ICM is many orders of magnitude larger than the kinetic scales of interest in this thesis, some observational proxy for the ICM plasma is essential to test our theory. The solar wind can be such a proxy, and some initial measurements seem to be in favor of our main conclusion [50]. To

further bring our theory in contact with the data we extended our results to lower-$\beta$ plasmas and discovered that electrostatic double layers, which manifest themselves at the Debye length of the plasma, are the primary means of suppressing heat flux. It was also shown that whistlers can damp and heat ions at the spatial scale of the electron gyroradius, while ion-acoustic shocklets from double layers can effect similar heating downstream of the double layer. These are examples of collisionless phenomena that couple the dynamics of ions and electrons and likely impact the behavior of the ICM at small scales.

## 5.2    Caveats

Our numerical model suffers from the common issue that, as Table 1.1 attests, the simulated length scales are dwarfed by the size of the astrophysical system we are trying to model. Furthermore, we have not incorporated weak collisions into our model which are an important ingredient in the real ICM. It is hard to determine how transport will be affected on global scales by the kinetic physics we have explored, although several authors have already made cases for how plasma instabilities could directly affect transport at astrophysically relevant scales [5, 17, 70].

## 5.3    Future Work

Several questions remain to be answered regarding the problem of thermal conduction in the ICM plasma. Since our 2D simulations conserve particle canonical momentum a next step would be to run 3D simulations to track the diffusion of particles perpendicular to $\mathbf{B}$. The physical picture outlined in chapter 3 suggests

that whistlers trap particles like buckets and move with their phase speed along and perpendicular to $B$. The oblique whistler propagation could therefore cause perpendicular transport, possibly of the same size as the parallel transport. Interactions with ion-scale heat fluxes and resulting wave modes remain to be studied. Adding collisions to the PIC model used would be a useful experiment that could place our theory closer to the true behavior of thermal conduction in the ICM.

An important case shown in this thesis is the relaxation of an initially imposed heat flux seen in Chapter 2. In that problem the oblique whistler amplitude is seen to decay at late time (Figure 2.4a), while the heat flux stays suppressed to some marginal level. Further recent observations of whistlers in the solar wind by Tong et al. [71] suggest that most of the fluctuations at 1 AU are parallel-propagating. However, this does not rule out the possibility that oblique whistlers can be locally generated by a large heat flux, relax the heat flux to a marginal level scaling as $1/\beta$ [50], and be damped by the plasma. This issue remains to be explored.

Finally, the physics of kinetic-scale thermal conduction could be added to MHD models of the ICM plasma as a so-called sub-grid prescription [37]. For the various processes mentioned in sec. 1.1.3 this new physics could significantly alter the role that thermal conduction plays in models of the ICM plasma.

# Bibliography

[1] L. S. Sparke and J. S. III Gallagher. *Galaxies in the Universe*. Cambridge University Press, 2007.

[2] A.~C. Fabian. Cooling Flows in Clusters of Galaxies. *Ara&a*, 32:277–318, 1994.

[3] Darren J. Croton, Volker Springel, Simon D.M. White, G. De Lucia, C. S. Frenk, L. Gao, A. Jenkins, G. Kauffmann, J. F. Navarro, and N. Yoshida. The many lives of active galactic nuclei: Cooling flows, black holes and the luminosities and colours of galaxies. *Monthly Notices of the Royal Astronomical Society*, 365(1):11–28, 2006.

[4] L. L. Cowie and J. Binney. Radiative regulation of gas flow within clusters of galaxies - A model for cluster X-ray sources. *The Astrophysical Journal*, 215:723, 1977.

[5] M. W. Kunz, A. A. Schekochihin, S. C. Cowley, J. J. Binney, and J. S. Sanders. A thermally stable heating mechanism for the intracluster medium: Turbulence, magnetic fields and plasma instabilities. *MNRAS*, 410(4):2446–2457, 2011.

[6] Nadia L Zakamska and Ramesh Narayan. MODELS OF GALAXY CLUSTERS WITH THERMAL CONDUCTION. *The Astrophysical Journal*, 582:162–169, 2003.

[7] C. S. Reynolds, S. Heinz, and M. C. Begelman. The hydrodynamics of dead radio galaxies. *Mon. Not. R. Astron. Soc.*, 332(2), 2002.

[8] A C Fabian, C S Reynolds, G B Taylor, and R J H Dunn. On viscosity, conduction and sound waves in the intracluster medium. *Mon. Not. R. Astron. Soc*, 363:891–896, 2005.

[9] Ellen G Zweibel, Vladimir V Mirnov, Mateusz Ruszkowski, Christopher S Reynolds, Karen Yang, and Andrew C Fabian. Acoustic Disturbances in Galaxy Clusters. *The Astrophysical Journal*, 858:5, 2018.

[10] Lennox L Cowie and Christopher F Mckee. THE EVAPORATION OF SPHER-ICAL CLOUDS IN A HOT GAS. I. CLASSICAL AND SATURATED MASS LOSS RATES. *The Astrophysical Journal*, 211:135–146, 1977.

[11] Eliot Quataert. BUOYANCY INSTABILITIES IN WEAKLY MAGNETIZED LOW-COLLISIONALITY PLASMAS. *The Astrophysical Journal*, 673:758, 2008.

[12] Steven A Balbus. Stability, Instability, and "Backward" Transport in Stratified Fluids. *The Astrophysical Journal*, 534:420–427, 2000.

[13] John A. ZuHone and Elke Roediger. *Cold fronts: probes of plasma astrophysics in galaxy clusters*, volume 82. 2016.

[14] A C Fabian, R M Johnstone, J S Sanders, C J Conselice, C S Crawford, J S Gallagher Iii, and E Zweibel. Magnetic support of the optical emission line filaments in NGC 1275. *Nature Letters*, 454:968–970, 2008.

[15] C. L. Carilli and G. B. Taylor. Cluster Magnetic Fields. 2001.

[16] L. Spitzer. *Physics of Fully Ionized Gases*. New York: Interscience, 2nd editio edition, 1962.

[17] F. Rincon, A. A. Schekochihin, and S. C. Cowley. Non-linear mirror instability. *MNRAS*, 447:L45–L49, 2014.

[18] S. Chapman and T. G. Cowling. *Mathematical Theory of Nonuniform Gases*. Cambridge University Press, 1953.

[19] S. I. Braginskii. Transport processes in a plasma, 1965.

[20] J V Hollweg. Electron Heat-Conduction in the Solar-Wind. *Journal of Geophysical Research*, 79(25):3845–3850, 1974.

[21] S. Peter Gary, Bullet W C Feldman, and D W Forslund. Heat Flux Instabilities in the Solar Wind. *Journal of Geophysical Research*, 80(31):4197, 1975.

[22] W. C. Feldman, J. R. Asbridge, S. J. Bame, and M. D. Montgomery. Solar wind heat transport in the vicinity of the Earth's bow shock. *Journal of Geophysical Research*, 78(19):3697–3713, 1973.

[23] Matthew W. Kunz, Alexander A. Schekochihin, and James M. Stone. Firehose and mirror instabilities in a collisionless shearing plasma. *Physical Review Letters*, 112(20):1–6, 2014.

[24] S V Komarov, E M Churazov, M W Kunz, and A A Schekochihin. Thermal conduction in a mirror-unstable plasma. *MNRAS*, 477:467–477, 2016.

[25] Shlomi Pistinner, Amir Levinson, and David Eichler. Can Electromagnetic Instabilities Driven By Temperature Gradients Inhibit Thermal Conduction in Cluster Cooling Flows? *The Astrophysical Journal*, 467:162–167, 1996.

[26] Benjamin D G Chandran and Steven C Cowley. Thermal Conduction in a Tangled Magnetic Field. *Physical Review Letters*, 80(14):3077–3080, 1998.

[27] Amir Levinson and David Eichler. Inhibition of electron thermal conduction by electromagnetic instabilities. *The Astrophysical Journal*, 387:212, 1992.

[28] S L Pistinner and D Eichler. Self-inhibiting heat flux. *Mon. Not. R. Astron. Soc.*, 301:49–58, 1998.

[29] S. Peter Gary, Earl E. Scime, John L. Phillips, and William C. Feldman. The whistler heat flux instability: Threshold conditions in the solar wind. *Journal of Geophysical Research*, 99(A12):23391, dec 1994.

[30] S. Peter Gary and Hui Li. Whistler Heat Flux Instability at High Beta. *The Astrophysical Journal*, 529(2):1131–1135, 2000.

[31] Mario A Riquelme, Eliot Quataert, and Daniel Verscharen. PIC SIMULATIONS OF THE EFFECT OF VELOCITY SPACE INSTABILITIES ON ELECTRON VISCOSITY AND THERMAL CONDUCTION. *The Astrophysical Journal*, 824, 2016.

[32] A. Ramani and G. Laval. Heat flux reduction by electromagnetic instabilities. *Physics of Fluids*, 21(6):980, 1978.

[33] Erich S. Weibel. Spontaneously growing transverse waves in a plasma due to an anisotropic velocity distribution. *Physical Review Letters*, 2(3):83–84, 1959.

[34] Burton D. Fried. Mechanism for Instability of Transverse Plasma Waves. *Physics of Fluids*, 2(3):337, 1959.

[35] H. Karimabadi, D. Krauss-Varban, and T. Terasawa. Physics of pitch angle scattering and velocity diffusion, 1. Theory. *Journal of Geophysical Research*, 97(A9):13853, sep 1992.

[36] N. A. Krall and A. W. Trivelpiece. *Principles of Plasma Physics*. San Francisco Press, 1986.

[37] S Komarov, A A Schekochihin, E Churazov, and A Spitkovsky. Self-inhibiting thermal conduction in a high-$\beta$, whistler-unstable plasma. *J. Plasma Phys*, 84(905840305), 2018.

[38] Gary R. Smith and Allan N. Kaufman. Stochastic Acceleration by a Single Wave in a Magnetic Field. *Physical Review Letters*, 34(26):1613, 1975.

[39] A. Zeiler, D. Biskamp, J. F. Drake, B. N. Rogers, M. A. Shay, and M. Scholer. Three-dimensional particle simulations of collisionless magnetic reconnection. *Journal of Geophysical Research*, 107(A9):1230, sep 2002.

[40] R. Mace, S. Dalena, and W. H. Matthaeus. Velocity space diffusion of charged particles in weak magnetostatic fields: Nonlinear effects, model constraints, and implications for simulations. *Physics of Plasmas*, 19(3), 2012.

[41] S. Dalena, a. Greco, a. Rappazzo, R. Mace, and W. Matthaeus. Magnetic moment nonconservation in magnetohydrodynamic turbulence models. *Physical Review E*, 86(1):1–13, 2012.

[42] H. Karimabadi, K. Akimoto, N. Omidi, and C. R. Menyuk. Particle acceleration by a wave in a strong magnetic field: Regular and stochastic motion. *Physics of Fluids B*, 2(3):606–628, 1990.

[43] Brett D Keenan and Mikhail V Medvedev. Diffusion and radiation in magnetized collisionless plasmas with small-scale Whistler turbulence. *Journal of Plasma Physics*, 82:905820207, 2016.

[44] K. M. Schoeffler, N. F. Loureiro, R. A. Fonseca, and L. O. Silva. The generation of magnetic fields by the Biermann battery and the interplay with the Weibel instability. *Physics of Plasmas*, 23(5), 2016.

[45] M. Ruszkowski and S. P. Oh. SHAKEN AND STIRRED: CONDUCTION AND TURBULENCE IN CLUSTERS OF GALAXIES. *The Astrophysical Journal*, 713:1332–1342, 2010.

[46] H.-Y. K. Yang and Christopher S. Reynolds. INTERPLAY AMONG COOLING, AGN FEEDBACK, AND ANISOTROPIC CONDUCTION IN THE COOL CORES OF GALAXY CLUSTERS. *The Astrophysical Journal*, 818(2):181, feb 2016.

[47] S. D. Bale, M. Pulupa, C. Salem, C. H. K. Chen, and E. Quataert. Electron Heat Conduction in the Solar Wind: Transition From Spitzer-Härm To the Collisionless Limit. *The Astrophysical Journal*, 769(2):L22, 2013.

[48] S Peter Gary, Jennifer A Newbury, and Bruce E Goldstein. Lower bound for electron core beta in the solar wind. *Journal of Geophysical Research*, 103(A7):559–566, 1998.

[49] S. Peter Gary, Elena Neagu, Ruth M Skoug, and Bruce E Goldstein. Solar wind electrons: Parametric constraints. *Journal of Geophysical Research*, 104(A9):19,843 – 19,849, 1999.

[50] Yuguang Tong, Stuart D. Bale, Chadi Salem, and Marc Pulupa. Observed instability constraints on electron heat flux in the solar wind. 2018.

[51] T C Li, J F Drake, and M Swisdak. SUPPRESSION OF ENERGETIC ELEC-TRON TRANSPORT IN FLARES BY DOUBLE LAYERS. *The Astrophysical Journal*, 757:20–7, 2012.

[52] T C Li, J F Drake, and M Swisdak. CORONAL ELECTRON CONFINEMENT BY DOUBLE LAYERS. *The Astrophysical Journal*, 778:144–9, 2013.

[53] T C Li, J F Drake, and M Swisdak. DYNAMICS OF DOUBLE LAYERS, ION ACCELERATION, AND HEAT FLUX SUPPRESSION DURING SO-LAR FLARES. *The Astrophysical Journal*, 793:7–7, 2014.

[54] O Buneman. Instability, Turbulence, and Conductivity in Current-Carrying Plasma. *Physical Review Letters*, 1:8, 1958.

[55] A. S. Volokitin and V. V. Krasnosel'skikh. Dynamic potential spikes due to the long-wave Buneman instability. *Soviet Journal of Plasma Physics*, 8(4):454, 1982.

[56] Lars P. Block. A Double Layer Review. *Astrophysics and Space Science*, 55:59, 1978.

[57] Nagendra Singh, H Thiemann, and R W Schunk. Electric fields and double layers in plasmas. *Laser and Particle Beams*, 5(2):233–255, 1987.

[58] M. A. Raadu and J. J. Rasmussen. Dynamical Aspects of Electrostatic Double Layers. *Astrophysics and Space Science*, 144:43, 1988.

[59] Eduard P Kontar, Nicolas H Bian, A Gordon Emslie, and Nicole Vilmer. TUR-BULENT PITCH-ANGLE SCATTERING AND DIFFUSIVE TRANSPORT OF HARD X-RAY-PRODUCING ELECTRONS IN FLARING CORONAL LOOPS. *The Astrophysical Journal*, 780:176, 2014.

[60] Aleksander Sadowski, Lorenzo Sironi, David Abarca, Xinyi Guo, Feryal ??zel, and Ramesh Narayan. Radio light curves during the passage of cloud G2 near Sgr A. *Monthly Notices of the Royal Astronomical Society*, 432:478–491, 2013.

[61] Lorenzo Sironi. ELECTRON HEATING BY THE ION CYCLOTRON IN-STABILITY IN COLLISIONLESS ACCRETION FLOWS. II. ELECTRON HEATING EFFICIENCY AS A FUNCTION OF FLOW CONDITIONS. *The Astrophysical Journal*, 800, 2015.

[62] P. A. Sturrock. Stochastic acceleration. *Physical Review*, 141(1):186–191, 1966.

[63] G. J. Morales and Y. C. Lee. Effect of Localized Electric Fields on the Evolution of the Velocity Distribution Function. *Phys. Rev. Lett.*, 33(26):1534, 1974.

[64] C Barnes, M K Hudson, and W Lotko. Weak double layers in ion-acoustic turbulence. *Phys. Fluids*, 28:1055, 1985.

[65] D. S. Main, D. L. Newman, C. Scholz, and R. E. Ergun. The formation and evolution of double layers inside the auroral cavity. *Geophysical Research Letters*, 40(12):2897–2901, 2013.

[66] R E Ergun, L Andersson, D Main, Y.-J Su, D L Newman, M V Goldman, C W Carlson, A J Hull, J P Mcfadden, and F S Mozer. Auroral particle acceleration by strong double layers: The upward current region. *J. Geophys. Res*, 109(A12220), 2004.

[67] S Peter Gary. The electron/electron acoustic instability. *The Physics of Fluids*, 30(9), 1987.

[68] Akira Hasegawa. Particle Acceleration by MHD Surface Wave and Formation of Aurora. *Journal of Geophysical Research*, 81(28):5083, 1976.

[69] Joseph V. Hollweg. Kinetic Alfvén wave revisited. *Journal of Geophysical Research: Space Physics*, 104(A7):14811–14819, 1999.

[70] A. A. Schekochihin, S. C. Cowley, R. M. Kulsrud, G. W. Hammett, and P. Sharma. PLASMA INSTABILITIES AND MAGNETIC FIELD GROWTH IN CLUSTERS OF GALAXIES. *The Astrophysical Journal*, 629:139–142, 2005.

[71] Yuguang Tong, Ivan Y Vasko, Marc Pulupa, Forrest S Mozer, Stuart D Bale, Anton V Artemyev, and Vladimir Krasnoselskikh. Whistler Wave Generation by Halo Electrons in the Solar Wind. *The Astrophysical Journal Letters*, 870:L6, 2019.